



# Peracetic acid-induced nanoengineering of Fe-based metallic glass ribbon in application of efficient drinking water treatment

Yujian Li<sup>a</sup>, Yan Liu<sup>b</sup>, Yangguang Zhan<sup>a</sup>, Yu Zhang<sup>a</sup>, Xingran Zhao<sup>a</sup>, Mengting Yang<sup>b</sup>, Wenqing Ruan<sup>a</sup>, Zhenxuan Zhang<sup>a,\*</sup>, Xiong Liang<sup>a,\*</sup>, Jiang Ma<sup>a,\*</sup>

<sup>a</sup> College of Mechatronics and Control Engineering, Shenzhen University, Shenzhen 518060, China

<sup>b</sup> College of Chemistry and Environmental Engineering, Shenzhen University, Shenzhen 518060, China

## ARTICLE INFO

### Keywords:

Glassy ribbon  
Advanced oxidation processes  
Disinfection by-products  
Peracetic acid  
Natural organic matter

## ABSTRACT

This study presents a novel approach utilizing Fe-Si-B metallic glass-based advanced oxidation processes (AOPs) with peracetic acid (PAA) exposure to mitigate disinfection by-products (DBPs) formation in drinking water treatment. Under optimal conditions, it achieved a 98.21% removal of natural organic matter (NOM) and an 80.64% reduction in DBPs formation. The efficacy is attributed to the galvanic cell effect induced by nanoflower structures on the ribbon surface, produced via PAA exposure, thereby enhancing degradation efficiency. High-valent iron Fe(IV) was identified as the primary reactive species, showing robust cycling efficiency under near-neutral conditions. Continuous flow experiments and toxicity assessments using luminescent bacteria further validated the method, demonstrating minimal metal leaching (<0.146 mg/L) and reduced biotoxicity with a 37.68% inhibition rate decrease in 24 h. These findings underscore the promising potential of PAA-integrated Fe-based amorphous alloys for comprehensive water disinfection and purification.

## 1. Introduction

Since the 1970s, the acceleration of industrial processes has led to a continuous increase in environmental pollution, with water pollution becoming a critical issue. Water pollution is negatively correlated with human health, making it essential to ensure the safety of drinking water [1]. The disinfection of drinking water to reduce waterborne diseases has been one of the significant achievements in public health in the 20th century [2]. During the process of converting surface water into drinking water, natural organic matter (NOM) emerges as a major source of pollution, primarily originating from humic substances such as decaying leaves and deceased organisms [3]. Chlorine-based disinfectants, which have been widely employed in drinking water treatment, could react with NOM and/or halide ions (bromide/iodide), giving rise to a series of disinfection by-products (DBPs) that pose a significant potential risk to human health [4]. Epidemiological studies have established a correlation between DBPs and various reproductive diseases, including adverse pregnancy outcomes and bladder cancer [5].

Since the first detection of trichloromethane in chlorinated drinking water in 1974, more than 800 DBPs have been identified successively [6]. Consequently, in the realm of drinking water treatment, there exists

a formidable challenge: maintaining disinfection efficacy while minimizing the generation of DBPs. Over the years, efforts have been dedicated to finding alternatives to chlorine disinfection to curtail the formation of halogenated DBPs. Peracetic acid (PAA), a chlorine-free disinfectant, has been integrated into drinking water disinfection due to its remarkable capacity to annihilate viruses and microorganisms [7, 8], while simultaneously averting the creation of chlorinated DBPs (Cl-DBPs) [9]. Nevertheless, recent work has brought to light the potential of PAA to oxidize bromide ions into hypobromous acid, thus giving rise to brominated DBPs (Br-DBPs) [10]. Consequently, the issue of generating DBPs when employing PAA for drinking water disinfection warrants further elucidation.

Fe-based materials have received extensive attention in the field of water treatment due to their affordability and superior treatment efficiency. Zero-valent iron (ZVI), iron oxides (FeO), bimetallic Fe-Cu catalysts, and Fe<sub>3</sub>O<sub>4</sub>/PMS/HA system based on the Fe(III)/Fe(II) cycle and the metal-free activation have been proved to effectively remove pollutants [11–14]. These Fe-based materials are crystalline in nature, while Fe-based amorphous alloys have received relatively less attention. Fe-based amorphous alloys are a unique type of ZVI material, obtained by rapidly cooling alloy atoms in a molten state, resulting in a

\* Corresponding authors.

E-mail addresses: [zxzhang@szu.edu.cn](mailto:zxzhang@szu.edu.cn) (Z. Zhang), [xliang@szu.edu.cn](mailto:xliang@szu.edu.cn) (X. Liang), [majiang@szu.edu.cn](mailto:majiang@szu.edu.cn) (J. Ma).

<https://doi.org/10.1016/j.apcatb.2024.124161>

Received 23 January 2024; Received in revised form 30 April 2024; Accepted 4 May 2024

Available online 9 May 2024

0926-3373/© 2024 Elsevier B.V. All rights reserved.

structurally disordered amorphous material [15]. Their special short-range ordered, long-range disordered atomic structure, and unique atomic coordination-induced electron transfer reactions enable them to maintain high activity in catalytic reactions by providing a stable catalytic environment [16,17]. Simultaneously, the residual stress, relaxation phenomena, and metastable characteristics that persist during the preparation of amorphous alloys bestow upon them a superior catalytic performance when compared to their crystalline counterparts [18,19]. The application of Fe-based amorphous alloys in water treatment has primarily focused on the activation of hydrogen peroxide or persulfate as oxidants for the degradation of dye wastewater and pollutants [20]. In contrast, PAA, as a crucial oxidant in advanced oxidation processes (AOPs), has been significantly underestimated.

PAA, with its excellent disinfection capabilities, deserves further investigation in conjunction with Fe-based amorphous alloys known for their catalytic performance in the context of drinking water treatment. In this study, Fe<sub>79</sub>Si<sub>9</sub>B<sub>13</sub> glassy ribbons were selected as the Fe-based amorphous material, with Fe<sub>79</sub>Si<sub>9</sub>B<sub>13</sub> crystalline ribbons and ZVI serving as comparisons. The study aims to investigate (1) their ability to remove NOM (humic acid) as precursors of DBPs, (2) their ability to control the generation of DBPs, (3) changes in the material's surface physicochemical properties, and (4) the generation of reactive species and mechanisms. The results obtained in this study are expected to further expand the application of Fe-based amorphous alloys in drinking water treatment and provide new strategies for controlling and removing DBPs, thus offering a novel candidate material for drinking water treatment.

## 2. Materials and methods

### 2.1. Materials

The hydrogen peroxide (H<sub>2</sub>O<sub>2</sub>, 30% w/w), humic acid (HA), acetonitrile (ACN), and methyl tert-butyl ether (MTBE) were purchased from Sigma-Aldrich. The acetic acid (99.8%), sodium chloride (NaCl, 98%), sodium bicarbonate (NaHCO<sub>3</sub>), sodium bromide (NaBr), sodium thiosulfate (Na<sub>2</sub>S<sub>2</sub>O<sub>3</sub>), sodium sulfate (Na<sub>2</sub>SO<sub>4</sub>), methyl phenyl sulfoxide (PMSO, 98%), methyl phenyl sulfone (PMSO<sub>2</sub>, 98%), sodium hypochlorite (NaClO, with 6–14% active chlorine), isopropanol (IPA, 99.5%), *tert*-butanol (TBA, 99.5%), methanol (MeOH, 99.5%), L-histidine (L-His, 99.5%), *p*-benzoquinone (*p*-BQ, 99%) and 5,5-dimethyl-1-pyrroline-N-oxide (DMPO) were obtained from Macklin (Shanghai, China). The sulfuric acid (H<sub>2</sub>SO<sub>4</sub>, 98%) was purchased from Xilong Chemical Co., Ltd. (Guangdong, China). The catalytic degradation experiments were carried out by using ultrapure water.

The preparation methods for the Fe-Si-B glassy ribbon and Fe-Si-B crystalline ribbon are detailed in Text S1 of [Supplementary material](#). The Fe ribbon (99.995%) with a thickness of 0.25 mm was obtained from Energy Chemical (Anhui, China). The Fe powder (99%, 100 mesh) was bought from Macklin (Shanghai, China).

### 2.2. Characterization of metal materials

The amorphous/crystalline structure of the surface of the Fe-Si-B glassy ribbon, crystalline ribbon and Fe ribbon was observed by X-ray diffraction analysis (XRD, Rigaku MiniFlex600) with Cu K $\alpha$  radiation. Nanoindentation (Bruker Hysitron TI980) was employed to measure the surface modulus distribution of the three materials. The surface composition and valence states of the different elements in the Fe<sub>79</sub>Si<sub>9</sub>B<sub>13</sub> glassy ribbons before and after the reaction were analyzed by X-ray photoelectron spectroscopy (XPS, Thermo Scientific K-Alpha). Scanning electron microscopy (SEM, FEI QUANTA FEG 650) equipped with an energy dispersive spectrometer (EDS) was used to determine the surface morphology and elemental information of the Fe-Si-B glassy ribbon under different reaction conditions. Inductively coupled plasma-Optical Emission spectroscopy (ICP-OES, Agilent 720ES) was employed

to quantify the leaching of Fe and Si during the catalysis reaction. Detailed information can be found in Text S2 of the [Supplementary material](#).

### 2.3. Preparation of simulated drinking water

The simulated raw water was prepared based on literature [21]. With the addition of humic acid at a concentration of 3 mg/L as C. To simulate the presence of CaCO<sub>3</sub>, NaHCO<sub>3</sub> was added at a concentration of 90 mg/L. NaBr was also added at a concentration of 0 or 2 mg/L to create a bromine-containing environment for the detection of Br-DBPs. The simulated raw water with a pH value of 7.4 was chlorinated to prepare simulated drinking water with chlorine doses of 5 mg/L Cl<sub>2</sub> and contact time of 2 h. NaClO (Macklin, 6–14% active chlorine basis, the stock solution concentration was measured by 4500-Cl F.DPD ferrous titration method) was used as the source of Cl<sub>2</sub> for disinfection. PAA was used as an oxidant for Fe-Si-B glassy ribbon-based AOPs. The detailed process for preparing the humic acid stock solution and PAA reagent can be found in Text S3 and S4 in the [Supplementary material](#).

The halogenated DBPs generated from chlorination/PAA oxidation of raw water in the presence of bromide were pre-concentrated by using liquid-liquid extraction (LLE) and analyzed by ultra pressure liquid chromatography – electrospray ionization – triple quadrupole mass spectrometry (UPLC-ESI-tqMS, Waters Xevo TQ-S). The detailed information for preparation, pretreatment of simulated drinking water and instrumental analysis can be found in Text S5 and S6 in the [Supplementary material](#).

### 2.4. Degradation of humic acid monitored by fluorimetry

To testify whether humic acid can be degraded by Fe-Si-B amorphous alloy-based AOPs (Fe-Si-B glassy ribbon + PAA), excitation-emission matrix (EEM) fluorescence spectroscopy was applied to monitor the concentration changes of humic acid during catalysis reaction. The experiments to study the degradation of humic acid were divided into two main groups and carried out under near neutral conditions. The first set of experiments was as follows: 300  $\mu$ mol/L PAA and 2 g/L Fe-Si-B glassy ribbon was sequentially added to 1 L of simulated drinking water, and reaction samples (2 mL) at different time intervals (0, 30, 60, 90, 120, and 150 min) were taken to obtain the fluorescence spectra. The solution needed to be filtered through a 0.22  $\mu$ m polyether sulfone (PES) membrane (Bojin, Tianjin) before measurement, after which it was placed on a fluorescence spectrophotometer (PerkinElmer FL8500) for EEM fluorescence measurement. The excitation spectrum (Ex) range was set from 240 to 650 nm and the emission spectrum (Em) range was set from 250 to 525 nm, respectively.

The effects of different dose of chlorination and PAA oxidation of humic acid were also investigated by EEM fluorescence as the second group of experiments. The simulated raw water (1 L) was chlorinated with Cl<sub>2</sub> concentrations of 0, 5, 10, and 20 mg/L for 12 h, respectively. Besides, the simulated raw water (1 L) was disinfected with PAA concentrations of 0, 5, 10, and 20 mg/L with and without the presence of 2 g/L of Fe-Si-B glassy ribbon for 12 h. The fluorescence measurement conditions are the same as the first set of fluorescence experiments.

### 2.5. Electron paramagnetic resonance (EPR) analysis of reactive species

The identification of reactive species was performed by using electron paramagnetic resonance (EPR) which utilizes spin trapping technology to allow for the detection of reactive free radicals by converting short-lived free radicals into longer-lasting paramagnetic groups [22]. The BRUKER EMX plus X-band spectrometer (Germany) was used for the detection of reactive species. The reaction samples of EPR experiments are generated by PAA and Fe-Si-B glassy ribbon exposure for some time, and then DMPO is added to trap reactive species. Then, a small amount of the solution is aspirated using a capillary and moved to the middle of

the tubing, where the end of the tubing is dipped in vacuum grease and sealed, and then placed in the EPR chamber for testing. The EPR detection parameters are: Center Field of 3500.00 G, Delay of 0.0 s, Static Field Mon of 3450.000 G, Sweep Width of 100.0 G, Width TM of 200.0 G, Frequency Mon of 9.818587 GHz, Power of 2.000 mW, Power Atten of 20.0 dB, Sweep Time of 60.00 s, Mod Freq of 100.00 kHz. The detailed procedures for EPR experiments can be found in Text S7 of the [Supplementary material](#).

## 2.6. Detection of PMSO and PMSO<sub>2</sub>

PMSO was selected as the chemical reagent to verify the existence of high-valent-iron Fe(IV). The experiments were performed as follows: PMSO (0.1 mmol/L), Fe-Si-B glassy ribbon (2 g/L), and PAA (10 mg/L) were sequentially added to initiate the reaction. At 0 min and 10 min of the reaction, 450  $\mu$ L of the reaction solution was taken to mix with 50  $\mu$ L of Na<sub>2</sub>S<sub>2</sub>O<sub>3</sub> (0.1 mmol/L) for quenching, and then 500  $\mu$ L of ultrapure water was added to mix uniformly and filtered with 0.22  $\mu$ m PTFE membrane before instrumental analysis. The detection of PMSO and PMSO<sub>2</sub> was performed by multiple reaction monitoring (MRM) mode in positive ion mode using UPLC-ESI-tqMS. BEH C18 (1.7  $\mu$ m, 2.1  $\times$  100 mm, Waters) column with a temperature of 35  $^{\circ}$ C was selected for UPLC separation. The mobile phases were water and methanol at a flow rate of 0.25 mL/min. The mobile phase was initially set to 0% methanol and 100% water, which was changed to 95% methanol and 5% water with the same gradient for the first 8 min, followed by a rapid return to 5% methanol and 95% water within 0.1 min, and then held for another 2.9 min. Product ion scanning (PIS) and multiple reaction monitoring (MRM) were used for structural confirmation and concentration calculations.

## 2.7. DFT calculation

The adsorption energies between PAA and three different materials were calculated based on density functional theory (DFT). The structural optimizations and electronic structure calculations are performed in the Vienna Ab Initio Simulation Package (VASP) code [23], based on the projector augmented wave (PAW) method with a cutoff energy of 300 eV [24]. All of configurations of FAPbI<sub>3</sub> based materials were fully optimized [23]. The generalized gradient form (GGA) of the exchange-correlation functional (Perdew-Burke-Ernzerhof 96, PBE) was adopted [25,26]. A revised Perdew-Burke-Ernzerhof generalized gradient approximation (PBEsol) [27,28] was used for the exchange-correlation. PBEsol functional has been introduced to improve the equilibrium properties of solids [29]. Valence-core interactions were described by projector-augmented-wave (PAW) pseudopotentials [30]. The Brillouin zone sampling is carried out using the (3  $\times$  3  $\times$  1) Monkhorst-Pack grids for surface and Gamma for the structure [24]. The convergence tolerance of energy is 1  $\times$  10<sup>-6</sup> eV, maximum force is 0.002 eV  $\text{\AA}^{-1}$ , and maximum displacement is 0.002  $\text{\AA}$  [24].

## 2.8. Overall toxicity evaluation

Luminescent bacteria (*Vibrio fischeri*) was selected to evaluate the overall toxicity of the samples during catalysis degradation [31]. The toxicity assessment experiment proceeded as follows: a bottle of lyophilized luminescent bacteria powder (Microtox® SOLO reagent) was quickly reconstituted with 2 mL of Microtox dilution solution, shaken to ensure even mixing, and then stored at 2–4  $^{\circ}$ C for 15 min until fully rehydrated. From various time intervals during catalytic degradation, 2 mL of sample solutions (pH 6–8) were collected. These samples were then filtered through a 0.22  $\mu$ m polyether sulfone (PES) membrane (Bojin, Tianjin). Subsequently, 50  $\mu$ L of Na<sub>2</sub>S<sub>2</sub>O<sub>3</sub> (0.01 mmol/L) was added to 1 mL of the filtered samples to neutralize any oxidants present. For the toxicity measurement, 100  $\mu$ L of the treated sample, 900  $\mu$ L of 2% (w/w) NaCl and 50  $\mu$ L of the bacterial solution were combined in a

cuvette. The mixture was shaken thoroughly and allowed to stand for 15 min before measuring on a TX-1315 toxicity analyzer (HACH). The results of the overall toxicity value for sample solutions acquired from different time intervals were expressed as the relative inhibitory rate (T %) of luminescent bacteria.

## 3. Results and discussion

### 3.1. Exposure to PAA results in the formation of nanostructures

The surface morphology of Fe-Si-B glassy ribbon exposed to PAA (5–20 mg/L) for 2 h was observed and analyzed by scanning electron microscopy (SEM). As shown in Fig. 1a, the original Fe-Si-B glassy ribbon sample (Control) had a predominantly smooth surface upon magnification. However, as depicted in Fig. 1b, exposure to 5 mg/L PAA transformed the ribbon's surface, making it rougher, and leading to the development of ductile cracks. Additionally, this concentration induced the formation of very fine nanoflowers on the surface due to oxidative erosion. In Fig. 1c, the exposure of 10 mg/L PAA resulted in the formation of large reaction pit prototypes (indicated by a yellow dotted line) and larger oxides with diameters around 2–3  $\mu$ m. These larger volumes of oxides arise from micro-galvanic cell reactions initiated by the nanoflowers, with corrosion products continuously adsorbing and accumulating. This phenomenon is indicative of the intensification of reactions with increasing PAA concentration. At a higher concentration of 20 mg/L PAA (Fig. 1d), a significant large pit formed on the ribbon's surface, surrounded by extensive oxides. This reaction process involves the growth and detachment of oxides, continuously exposing unreacted areas and creating new reaction sites, thus leading to the formation of surface pits and enhanced nanoflower production. These newly formed pits and nanostructures like nanoflowers could possibly contribute to improved catalysis degradation efficiency of humic acid. Further investigations into the structural origins of the Fe-Si-B glassy ribbon's high catalytic activity were conducted by measuring the water contact angles under the four different PAA exposure concentrations after 12 h (Fig. 1e). The original glassy ribbon exhibited a contact angle of 58.9 $^{\circ}$ , whereas the ribbons treated with 5 mg/L, 10 mg/L, and 20 mg/L PAA displayed contact angles of 5.5 $^{\circ}$ , 4.8 $^{\circ}$ , and 4.1 $^{\circ}$ , respectively. To investigate the reasons for the enhanced hydrophilicity of the Fe-Si-B glassy ribbon upon exposure to PAA, changes in the contact angle of the Fe-Si-B crystalline ribbon in relation to their morphological changes observed by SEM were also examined and the results are presented in Fig. S1. The water contact angle of the original glassy ribbon was 60.2 $^{\circ}$ . After a 30-minute exposure to 10 mg/L PAA, the contact angle decreased sharply to 5.2 $^{\circ}$ , which corroborated the aforementioned measurements. In contrast, the water contact angle of the original crystalline ribbon changed from 62.8 $^{\circ}$  to 40.7 $^{\circ}$  under the same conditions. The respective SEM images confirmed that the crystalline ribbon only exhibited increased grain precipitation after the reaction, with no formation of nanoflowers on the surface (Fig. S1). These findings suggest that the nanostructures formed by the glassy ribbon (i.e., nanoflower) fundamentally alter surface roughness, rendering the glassy ribbon highly hydrophilic. Importantly, the formation of nano-patterns on the Fe-Si-B glassy ribbon's surface during the reaction generates a potential difference, which facilitates the formation of galvanic cells, which will be discussed later. This enhanced hydrophilicity facilitates more effective contact between the solution and active sites within the reaction system, fostering a galvanic cell effect. This effect could potentially accelerate the catalytic degradation rate, establishing the Fe-Si-B glassy ribbon as an efficient catalyst.

### 3.2. The degradation of humic acid

EEM fluorescence was applied to monitor the concentration changes of humic acid during catalysis degradation by Fe-Si-B amorphous alloys-based AOPs. As shown in Fig. 2a, the fluorescence intensity of humic



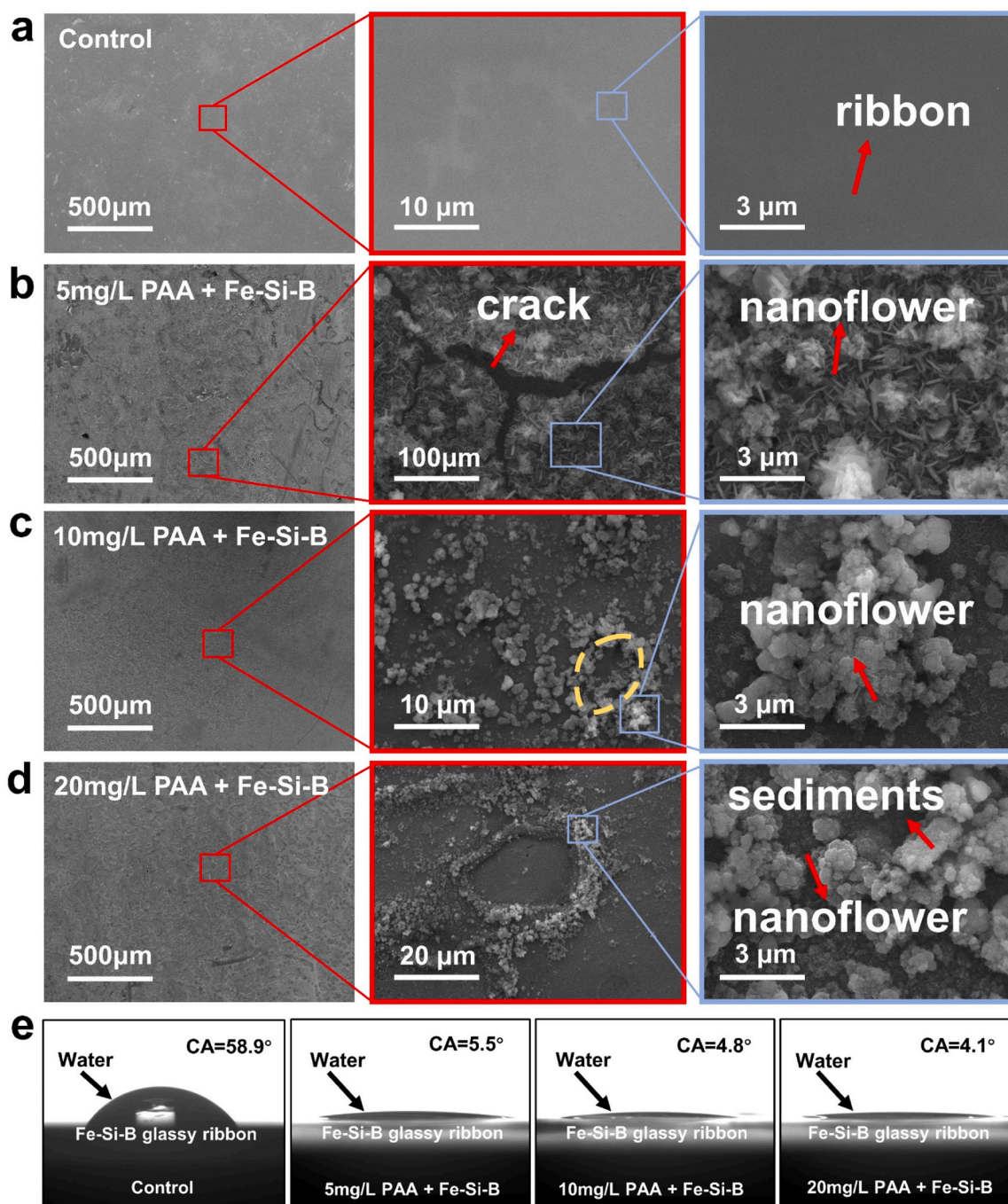


**Fig. 1.** (a) The SEM image of the as-received Fe-Si-B glassy ribbon, (b-d) The SEM images of Fe-Si-B glassy ribbon (Fe-Si-B = 2 g/L) exposure to PAA by doses of 5, 10, and 20 mg/L, (e) Contact angle of water droplets of Fe-Si-B glassy ribbon exposure to four doses of PAA (0, 5, 10, and 20 mg/L).

acid which appeared at the wavelength of  $\lambda_{\text{ex}} = 250 \text{ nm}$ ,  $\lambda_{\text{em}} = 450 \text{ nm}$  (region V) [32] continuously decayed during the reaction process. At time of 0 min, the color chart of the fluorescence spectrum was dark red, with a fluorescence signal intensity of about 21009. After 30 min of reaction, the signal intensity of humic acid in simulated raw water was about 5045, and the degradation efficiency was up to 75.99%, with the fluorescence spectrum turning light blue. After 150 min of reaction, the signal intensity of humic acid in the same region dropped to about 1320, and the degradation efficiency reached 93.71%, with the fluorescence spectrum turning blue. The results showed that the Fe-Si-B glassy ribbon combined with system could rapidly degrade humic acid.

Since PAA itself can react with humic acid, the decay of humic acid by PAA alone was investigated to measure its contribution to the

deduction of humic acid. Besides,  $\text{Cl}_2$  disinfection (used as  $\text{NaClO}$ ), as a drinking water disinfectant required in daily life, has high disinfection efficiency and is a common method for treating drinking water. The decay of humic acid by  $\text{Cl}_2$  disinfection (used as  $\text{NaClO}$ ) was applied as a comparison. By comparing the disinfection performance of PAA and  $\text{Cl}_2$ , it has been proved that one dose of  $\text{Cl}_2$  is equivalent to two doses of PAA [33], so two doses of PAA were chosen to be compared with one dose of  $\text{Cl}_2$ . The degradation processes of humic acid by chlorination disinfection, PAA disinfection and PAA combined with Fe-Si-B glassy ribbon are shown in Fig. 2b and Fig. S2 in the Supplementary material. The experimental results showed that the  $\text{Cl}_2$  disinfection (Fig. S2a) could reduce the humic acid as the  $\text{Cl}_2$  concentration increased, but the degradation effect was not strong enough. The PAA alone (Fig. S2b)



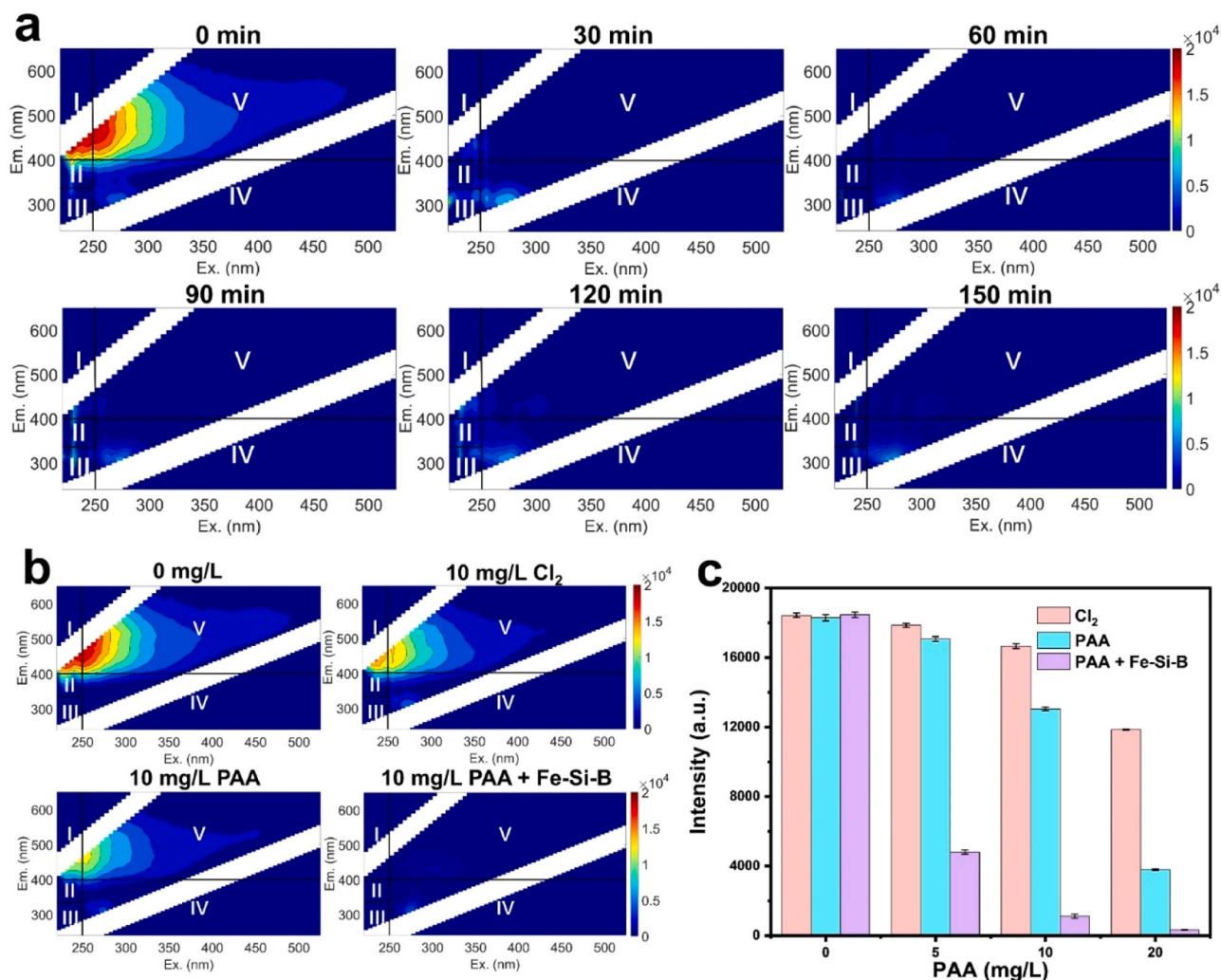


**Fig. 2.** (a) Fluorescence EEM spectra of humic acid in the presence of PAA ([PAA]<sub>0</sub> = 300 μmol/L) and Fe-Si-B glassy ribbon (ribbon dosage 2 g/L) at 0, 30, 60, 90, 120, and 150 min, (b) Fluorescence EEM spectra of humic acid with the addition of the same dose (10 mg/L) of oxidants (the addition of Fe-Si-B ribbon is 2 g/L), (c) Histogram of the fluorescence intensity by different oxidation treatment processes.

could reduce the humic acid signal intensity as the PAA concentration increased, with a stronger degradation effect than the Cl<sub>2</sub> system (Fig. S2a). As shown in Fig. S2c, The PAA combined with Fe-Si-B glassy ribbon significantly reduced the humic acid signal intensity as the PAA concentration increased, with the fluorescence spectrum turning blue overall at PAA concentration of 5 mg/L and almost completely blue at PAA concentration of 20 mg/L. The effectiveness of the catalysis degradation reaction was shown in Fig. 2c. The average initial humic acid fluorescence signal intensity of the simulated raw water uniformly configured was about 18,335. When measured with chlorination dose of 20 mg/L, after 12 h of reaction, the humic acid fluorescence signal intensity was about 11,850, with a residual degradation content of about 35.37%. The humic acid fluorescence signal intensity by PAA alone was about 3793, with a degradation effect of about 79.31%. The humic acid fluorescence signal intensity in the PAA combined with Fe-Si-B glassy ribbon was about 328, with a degradation effect of about 98.21%. These results indicated that the combination of PAA with the Fe-Si-B glassy ribbon system exhibited superior degradation effects on humic acid compared to the use of PAA or Cl<sub>2</sub> alone, demonstrating remarkable efficacy.

### 3.3. Formation control of DBPs by three materials

The EEM fluorescence results have demonstrated the excellent

performance of PAA combined with the Fe-Si-B glassy ribbon in degradation of humic acid. The formation control of DBPs were investigated by using UPLC-ESI-tqMS. By conducting precursor ion scan mode of  $m/z = 79/81$  (natural isotopes of Br), all polar brominated DBPs can be measured in one scan [34]. As a chlorine-free disinfection reagent, the different types of generated DBPs between PAA disinfection and Cl<sub>2</sub> disinfection of simulated raw water was firstly compared. The results indicated that the generation of DBP types changed dramatically from Cl<sub>2</sub> to PAA. Fig. 3 illustrates a comparative analysis of the DBP types generated by Cl<sub>2</sub> and PAA disinfection. Through Cl<sub>2</sub> disinfection, chlorobromoacetic acid (171/173/175), 2-bromobutenedioic acid (193/195), dichlorobromoacetic acid (205/207/209/211), dibromoacetic acid (215/217/219), 3,3-dibromopropenoic acid (227/229/231) and 3,5-dibromosalicylic acid (293/295/297) were formed (Fig. 3a). By contrast, 2-bromobutenedioic acid (193/195), dichlorobromoacetic acid (205/207/209/211), dibromoacetic acid (215/217/219), 3,3-dibromopropenoic acid (227/229/231), bromo-propyl-benzenediol (229/231), and dibromo-2,4-hexadienoic acid (267/269/271) were formed by PAA disinfection (Fig. 3b). It can be also seen from Fig. 3c that PAA disinfection generated relatively less DBPs compared to Cl<sub>2</sub> disinfection calculated by the total ion intensity (TII) of  $m/z = 79/81$ . Detailed information, including retention time, and  $m/z$  value of the DBPs, are provided in Tables S1-S2.

The formation control performance of DBPs catalyzed by PAA

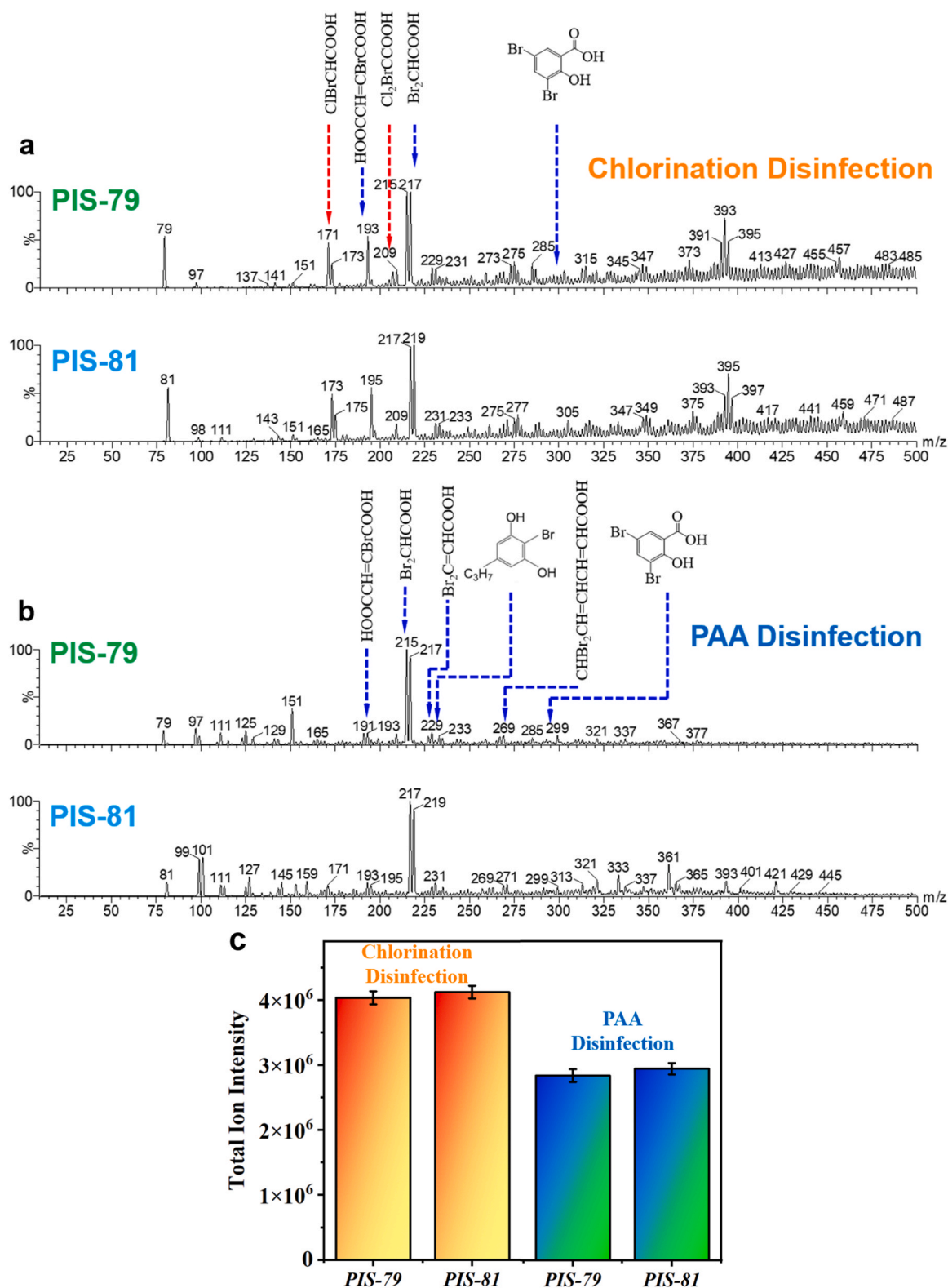
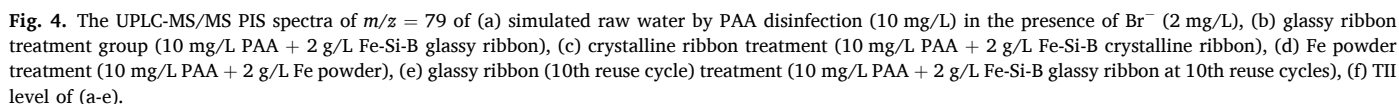


**Fig. 3.** The UPLC-MS/MS PIS spectra of (a)  $m/z = 79$  and  $m/z = 81$  of simulated raw water by  $\text{Cl}_2$  disinfection (5 mg/L) in the presence of  $\text{Br}^-$  (2 mg/L), (b)  $m/z = 79$  and  $m/z = 81$  of simulated raw water by PAA disinfection (10 mg/L) in the presence of  $\text{Br}^-$  (2 mg/L), (c) Comparison of the TII level of the PIS  $m/z = 79/81$  of (a) and (b).

combined with Fe-Si-B glassy ribbon was investigated based on comparison with DBPs formed by PAA disinfection of simulated raw water. As the TII level accumulated from precursor ion scans of  $m/z = 79$  can reflect the total amount of DBPs in the water sample, the formation control efficiency was calculated based on TII level. Besides, Fe-Si-B

crystalline ribbon and ZVI powder was also selected to test their control performance of DBPs as comparisons with the aim to offer critical insights into the effectiveness and potential benefits of Fe-Si-B glassy ribbon. As shown in Fig. 4, the PAA combined with Fe-Si-B glassy ribbon exhibited superior performance over Fe-Si-B crystalline ribbon and ZVI





powder, with their TII level ranked as follows: Fe-Si-B glassy ribbon < Fe-Si-B crystalline ribbon < ZVI powder (Fig. 4f). This hierarchy underscores the reduced DBP formation by PAA disinfection compared to  $\text{Cl}_2$  disinfection and indicates that adding different catalysts variably enhances degradation capabilities. Notably, Fe-Si-B glassy ribbon also demonstrated improvement in degradation performance after ten reaction cycles, highlighting the system's effectiveness and reusability.

To delve deeper into the underlying mechanisms behind the exceptional performance of Fe-Si-B glassy ribbon, a comprehensive examination of the changes in the surface physicochemical properties of the three materials involved was conducted by using surface morphology, nanoindentation, and electrochemical analysis. Regarding the surface morphology, as shown in Fig. 5a, the Fe-Si-B glassy ribbon exhibits a very smooth texture prior to the reaction. Post-reaction, however, the surface undergoes significant changes, characterized by the formation of cracks and pits. Furthermore, the surface is embellished with an array of nano-patterns, a transformation that significantly expands the specific surface area, as evidenced by the results of the contact angle measurements in the previous discussion. In the case of the Fe-Si-B crystalline ribbon, post-reaction observations revealed an increase in the number of precipitated grains on the surface. However, unlike its glassy counterpart, the crystalline ribbon did not exhibit the formation of nano-structures on its surface. In contrast, for ZVI powder, there is little to no observable change in the surface morphology following the reaction.

Given that the catalytic reaction occurs on the surface of the ribbon, the adsorption energy between the material and PAA could be a significant factor influencing the degradation performance. The adsorption energy ( $E_{ad}$ ) between each material and PAA was calculated and compared based on density functional theory (DFT). As shown in Fig. 5b,  $E_{ad}$  of Fe-Si-B amorphous alloy, crystalline alloy and pure Fe towards PAA are  $-2.251$ ,  $-2.193$  and  $-2.029$  eV, respectively. The order of magnitude for the  $E_{ad}$  follows the order: Fe-Si-B amorphous alloy > Fe-Si-B crystalline alloy > pure Fe. This indicates that the unique structure of Fe-Si-B amorphous alloy facilitates more efficient adsorption of PAA compared to the other materials. Enhanced adsorption of PAA is conducive to the reaction between  $\text{Fe}^{2+}$  and PAA, leading to the formation of reactive species  $\text{Fe(IV)}$ , as discussed later. The XRD spectra of the three materials before and after reaction are presented in Fig. 5c and Fig. 5d, respectively. The results demonstrate that the Fe-Si-B glassy ribbon maintains its amorphous characteristics post-reaction, while the properties of Fe-Si-B crystalline ribbon and Fe powder remain unchanged as well. Regarding the atom activity of the three materials, their modulus distribution were further investigated by nanoindentation and the results show that the modulus distribution on the surface of Fe-Si-B glassy ribbon has the narrowest modulus distribution, following the order: Fe-Si-B glassy ribbon < Fe-Si-B crystalline ribbon < Fe ribbon (Fig. 5e), which calculated from the modulus mapping of Fe-Si-B glassy ribbon (Fig. 5f), Fe-Si-B crystalline ribbon (Fig. 5g), and Fe ribbon (Fig. 5h). This suggests that the Fe-Si-B glassy ribbon exhibits active dynamic behavior. Notably, its surface features an active "liquid-like" layer, within which  $\text{Fe}^{2+}$  demonstrates remarkable reactivity. This  $\text{Fe}^{2+}$  is readily oxidized by PAA to form reactive species, indicating a high potential for catalytic activity.

Electrochemical tests were conducted to analyze the electron transfer state of the three materials during the catalytic reaction. Analysis of the cyclic voltammetry (CV) curves for the three materials (Fig. 5i) reveals that initially, the Fe ribbon is the most prone to oxidation owing to its strong reducing ability. However, as the reaction progresses, the oxidation potential of the Fe-Si-B glassy ribbon at  $-0.35$  V surpasses that of the Fe ribbon possibly result from the generation of nanostructures on Fe-Si-B glassy ribbon during catalysis reaction. Electrochemical impedance spectroscopy data (Fig. 5j) shows that in the high-frequency region, the resistance values follow the order:  $R_{\text{Fe-Si-B glassy ribbon}} < R_{\text{Fe-Si-B crystalline ribbon}} < R_{\text{Fe ribbon}}$ . This suggests that the amorphous alloys exhibit the highest charge transfer efficiency in PAA-catalyzed oxidation reactions, likely due to increased surface area from micro-nano structures

and the galvanic cell effect. Additionally, Tafel curve analysis (Fig. 5k) indicates a corrosion current order of Fe-Si-B glassy ribbon < Fe-Si-B crystalline ribbon < Fe ribbon, highlighting the superior corrosion resistance and recyclability of the Fe-Si-B glassy ribbon as a catalytic material. The galvanic cell effect describes a phenomenon wherein the formation of micro-nanostructures on the surface of Fe-based amorphous alloys induces localized potential differences, leading to electron flow between different regions of the material. This effect can boost degradation efficiency by facilitating redox reactions. Electrochemical analysis of the Fe-Si-B glassy ribbon revealed it exhibited the highest charge transfer efficiency (as shown in Fig. 5i-k) and the most straightforward adsorption in the PAA-catalyzed oxidation reaction. In these electrochemical cells, Fe serves as the more reactive cathode, donating electrons, while the less reactive Si acts as the anode, accepting electrons. This configuration establishes a galvanic cell, allowing Fe to continuously release a significant number of electrons at a much faster rate than in reactions involving only  $\text{Fe}^0$ . As a result, this mechanism enhances the degradation efficiency. These findings suggest that the Fe-Si-B glassy ribbon exhibits a higher affinity for binding and reacting with PAA. This enhanced interaction facilitates the formation of micro-nanostructures which induces galvanic cell effect, thereby improving the degradation efficiency and exerting more effective control over the formation of DBPs.

### 3.4. Characterization of metal materials before and after catalysis reaction

To gain a more comprehensive understanding of the good catalytic performance of the Fe-Si-B glassy ribbon, energy dispersive spectrometer (EDS) and X-ray photoelectron spectroscopy (XPS) are conducted to analyze changes in the surface physicochemical properties.

#### 3.4.1. EDS analysis

Given the observed alterations in the surface morphology of the Fe-Si-B glassy ribbon, it becomes imperative to examine the changes in its elemental composition before and after the catalysis reaction. Therefore, employing an EDS to scrutinize areas of interest such as pits and cracks on the ribbon's surface is essential for a thorough and detailed understanding. As shown in Fig. 6 and Table 1, the analysis of the Fe-Si-B glassy ribbon reveals interesting changes in the elemental composition due to the reaction with PAA at different concentrations. Initially, the Fe-Si-B glassy ribbon has a smooth surface, with the Fe content (81.71%) significantly higher than Si (8.31%), closely matching its designed atomic ratio (78: 9). Upon reaction with PAA at 5 mg/L, both Fe and Si contents decrease, with Fe dropping to 73.41% and Si to 8.09%, while O content increases to 12.56%. This suggests that the reaction leads to some leaching of Fe and Si atoms, and the formation of surface deposits that increase the oxygen content. As the concentration of PAA increases to 10 mg/L, the leaching effect becomes more pronounced. The Fe content further decreases to 71.74% and Si to 7.42%, while O content rises to 13.37%. This trend continues with PAA at 15 mg/L, leading to Fe content dropping to 67.54%, Si to 6.87%, and an increase in O content to 16.23%. Despite these changes, the atomic ratio of Fe to Si remains roughly around the initial ratio, indicating that both elements are leaching at a similar rate. These results demonstrate that the Fe-Si-B glassy ribbon's elemental composition is affected by the concentration of PAA, with higher concentrations leading to increased leaching of Fe and Si and more oxygen deposition. This highlights the ability of PAA to activate and affect the Fe-Si-B glassy ribbon, potentially impacting its catalytic properties in water treatment applications.

#### 3.4.2. XPS analysis

As displayed in Fig. 7, the XPS analysis of the Fe-Si-B glassy ribbon provides detailed insight into how its surface chemistry changes in response to the addition of PAA at varying concentrations. Initially, the pristine Fe-Si-B glassy ribbon shows characteristic peaks for B-B

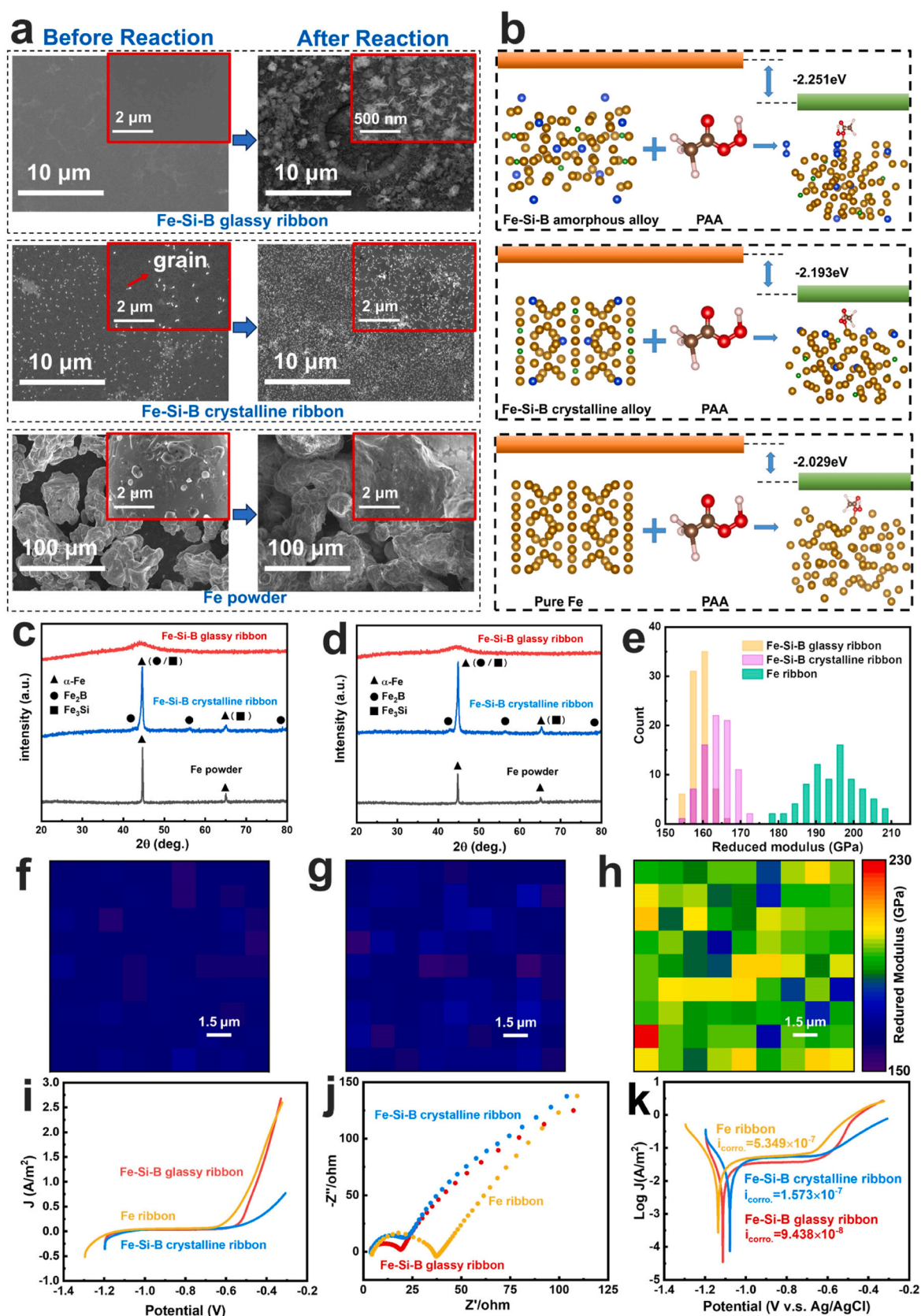


**Fig. 5.** (a) SEM images of Fe-Si-B glassy ribbon, Fe-Si-B crystalline ribbon and Fe powder before and after exposure to PAA (10 mg/L) for 2 h, (b) DFT calculation results of adsorption energy of Fe-Si-B amorphous alloy, Fe-Si-B crystalline alloy and pure Fe over PAA, (c-d) XRD results of Fe-Si-B glassy ribbon, Fe-Si-B crystalline ribbon and Fe powder before and after catalysis reaction, (e) Modulus distribution histogram of Fe-Si-B glassy ribbon, Fe-Si-B crystalline ribbon and Fe ribbon, (f-h) The dynamic modulus mapping of Fe-Si-B glassy ribbon, Fe-Si-B crystalline ribbon and Fe ribbon, (i-k) CV curves, Nyquist plots and Tafel curves of Fe-Si-B glassy ribbon, Fe-Si-B crystalline ribbon and Fe ribbon ( $[\text{Na}_2\text{SO}_4 \text{ electrolyte}]_0 = 0.05 \text{ M}$ ).



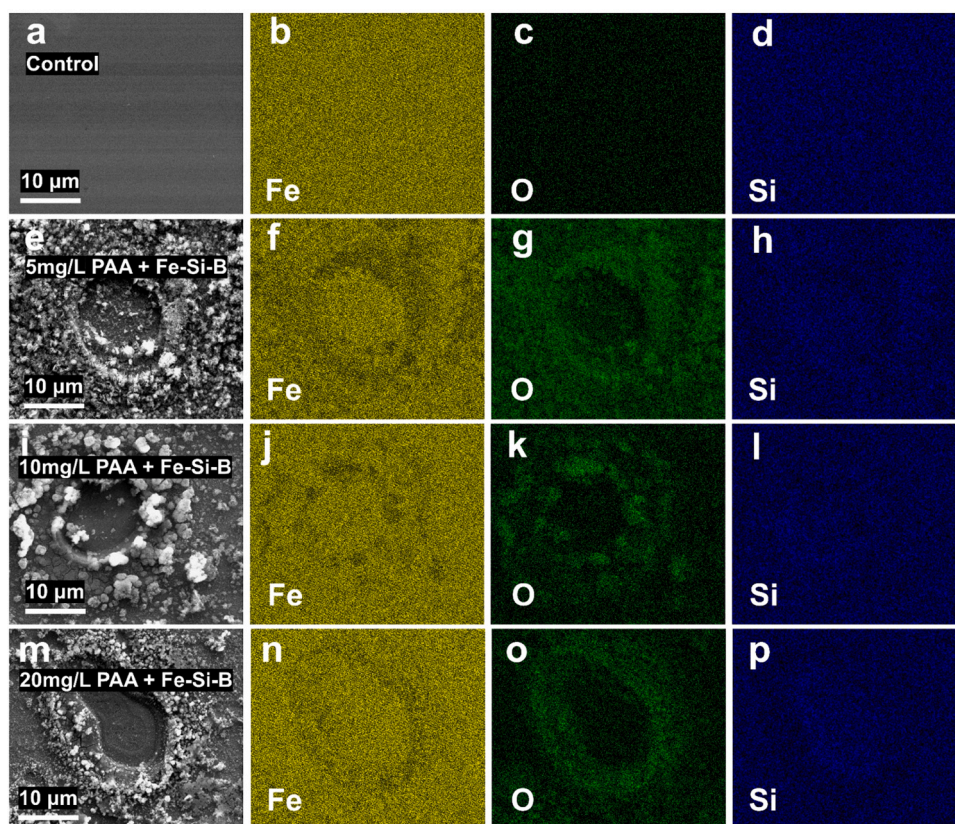


**Fig. 6.** (a-d) The EDS spectra of the as-received Fe-Si-B glassy ribbon and the elemental distribution of Fe, O, and Si, (e-h) The EDS spectra of the Fe-Si-B glassy ribbon with addition of 5 mg/L PAA and the elemental distribution of Fe, O, and Si, (i-l) The EDS spectra of the Fe-Si-B glassy ribbon with addition of 10 mg/L PAA and the elemental distribution of Fe, O, and Si, (m-p) The EDS spectra of the Fe-Si-B glassy ribbon with addition of 20 mg/L PAA and the elemental distribution of Fe, O, and Si.

**Table 1**  
EDS analysis of Fe-Si-B glassy ribbon reacting with different doses of PAA.

Element (Atom %)	Fe-Si-B	5 mg/L PAA + Fe-Si-B	10 mg/L PAA + Fe-Si-B	20 mg/L PAA + Fe-Si-B
C K	03.27	05.94	07.47	09.35
O K	06.71	12.56	13.37	16.23
Si K	08.31	08.09	07.42	06.87
Fe K	81.71	73.41	71.74	67.54

(186.38 eV), B-O (190.68 eV), Si-Si (97.98 eV), Si-O (100.88 eV), Fe-O (528.48 eV), C-O (530.18 eV), and different oxidation states of iron [ $\text{Fe}^0$  (705.68 eV, 28.09%),  $\text{Fe}^{2+}$  (709.08 eV, 44.45%),  $\text{Fe}^{3+}$  (711.18 eV, 27.46%)]. This initial composition sets the baseline for observing changes post-reaction. Fig. 7e-h shows the received XPS results of B 1 s, Si 2p, O 1 s, Fe 2p after addition of 5 mg/L PAA reacted with Fe-Si-B glassy ribbon. The results show that the relative contents of B-O and B-B bonds decreased by about 35.27%, and the total contents of Si-O and Si-Si decreased by about 54.86%, indicating some Si atoms exuded which possibly helps the formation of nanoflower structure. The participation of Fe-Si-B glassy ribbon in the reaction results in the formation of hydroxylated iron oxides ( $\text{FeOOH}$ ), and the ratio of the C-O peak area decreased dramatically. The original content of  $\text{Fe}^0$  became 0% after reaction, while the peak areas of both  $\text{Fe}^{2+}$  and  $\text{Fe}^{3+}$  increased to different degrees, but the total amount of Fe decreased by 21.20%, indicating a significant amount of Fe leaching involved in the reaction. Fig. 7i-l gives the received XPS results of B 1 s, Si 2p, O 1 s, Fe 2p after the addition of 10 mg/L PAA reacted with Fe-Si-B glassy ribbon. The results showed that the total content of B-O and B-B bonds decreased by

about 54.45%, the number of amorphous structures of B atoms destroyed was very high, and the total content of Si-O and Si-Si decreased by about 58.57%. Fe atoms were involved in the generation of hydroxylated iron oxide ( $\text{FeOOH}$ ), and the originally contained  $\text{Fe}^0$  completely disappeared with the total amount of Fe decreased by 22.64%. Fig. 7m-p gives the received XPS results of B 1 s, Si 2p, O 1 s, and Fe 2p after the addition of 20 mg/L PAA reacted with Fe-Si-B glassy ribbon are given. The results showed a decrease of about 38.12% in the total amount of B-O and B-B bonds, and a decrease of about 57.31% in the total amount of Si-O and Si-Si, proving that the Si leaching almost stabilizes around 10 mg/L PAA exposure.  $\text{Fe}^0$  also completely disappeared, and the total amount of Fe decreased by 28.31%, and the Fe leaching increases with the increase of the PAA concentration. These results demonstrate that the reaction with PAA not only affects the surface chemistry of the Fe-Si-B glassy ribbon but also leads to substantial changes in the elemental composition, particularly in the iron content and oxidation state. The disappearance of  $\text{Fe}^0$  and the formation of Fe oxides and  $\text{FeOOH}$  suggest that the amorphous matrix of the ribbon serves as an electron supplier during the catalytic process. It is noteworthy that the total amount of B-O and B-B bonds decreased after the addition of different doses of PAA. As a crucial component of the Fe-Si-B glassy ribbon, boron warrants particular attention. Due to its low standard potential ( $E^0 = -0.87$  V vs SHE), boron plays a central role in the corrosive behavior and the addition of boron will inhibit the formation of a dense oxide layer at the metal-water interface [35,36]. The formed incompact oxide layer would decrease the obstacle of the electron transfer from the metal to the pollutant. Besides, a recent study by Zhou et al. also demonstrated that boron as a green electron-sacrificer is an ideal and promising metal-free sacrifier to indirectly accelerate  $\text{Fe(III)}$  reduction for sustainable regeneration of  $\text{Fe(II)}$  in Fenton-like chemistry



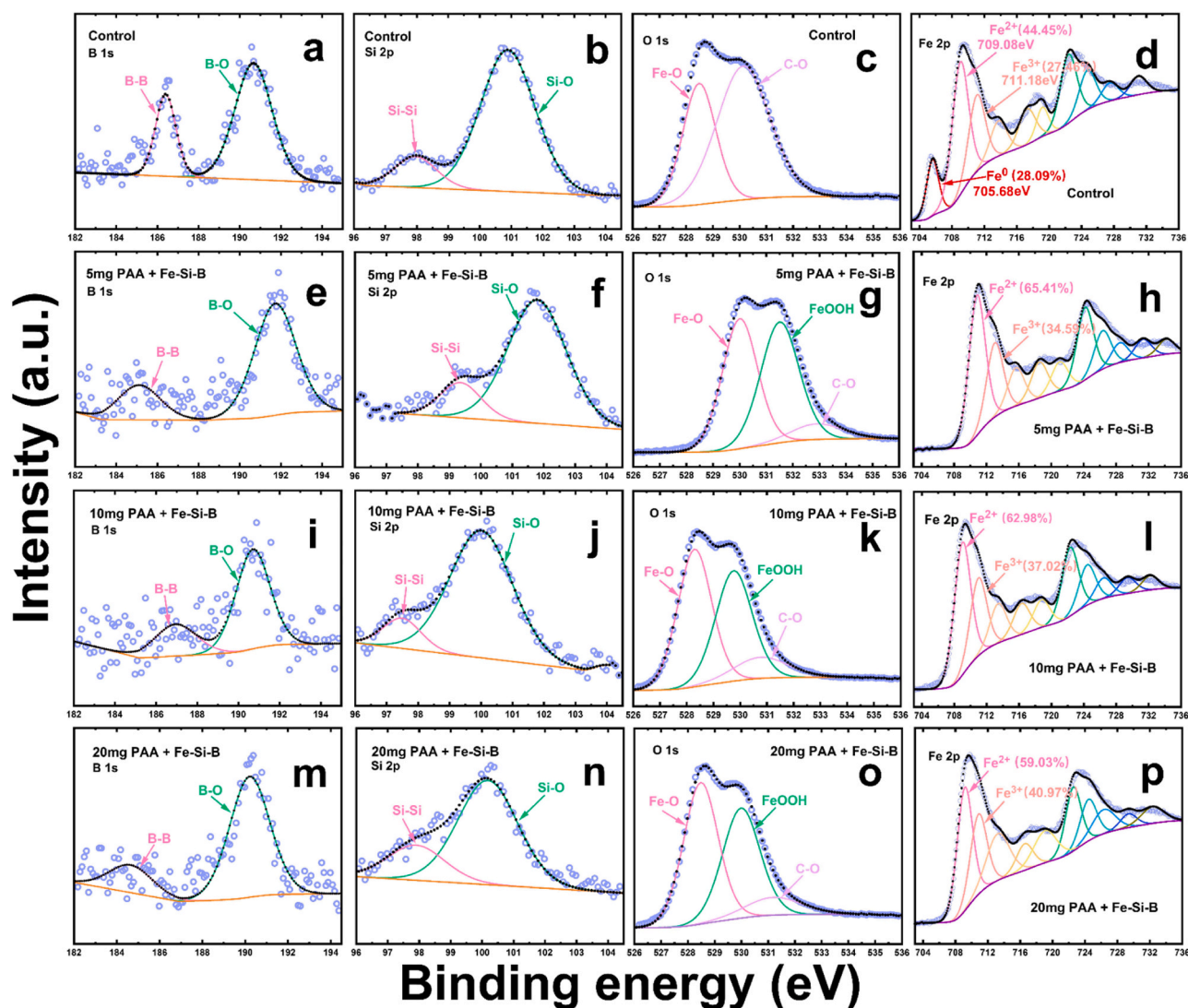


**Fig. 7.** The XPS spectra of (a-d) B 1s, Si 2p, O 1s, and Fe 2p for the as-received Fe-Si-B glassy ribbon, (e-h) B 1s, Si 2p, O 1s, and Fe 2p for the Fe-Si-B glassy ribbon with addition of 5 mg/L PAA, (i-l) B 1s, Si 2p, O 1s, and Fe 2p for the Fe-Si-B glassy ribbon with addition of 10 mg/L PAA, (m-p) B 1s, Si 2p, O 1s, and Fe 2p for the Fe-Si-B glassy ribbon with addition of 20 mg/L PAA.

[37]. The increasing leaching of Fe and Si with higher PAA concentrations indicates that the ribbon's catalytic properties are closely tied to these compositional changes.

### 3.5. Identification of reactive species

The reactive species responsible for the catalysis reaction are identified by EPR. As shown in Fig. 8a, the characteristic signals of DMPO-OH (blue circle) and HDMPO-OH (red square), with peak ratios of 1:2:2:1 and 1:1:1:1 (green line), respectively can be produced after 3 minutes reaction of Fe-Si-B glassy ribbon with PAA. From Fig. S3, it's inferred that DMPO-OH interacts with  $\text{Fe}^{n+}$ , releases  $\text{H}^+$ , adds electrons to  $\text{Fe}^{n+}$  to form  $\text{Fe}^{(n-1)+}$ , and separates from  $\text{Fe}^{(n-1)+}$ , and then forms HDMPO-OH. The above two sets of experiments showed that there were reactive species such as  $\bullet\text{OH}$  or  $\text{Fe(IV)}$  in the Fe-Si-B glassy ribbon-based AOPs to convert DMPO-OH to HDMPO-OH. IPA could act as a strong scavenger of  $\bullet\text{OH}$  and has a high reaction rate with  $\bullet\text{OH}$  ( $k = 9.7 \times 10^8 \text{ M}^{-1}\text{s}^{-1}$ ) [38,39]. In order to explore whether  $\bullet\text{OH}$  or  $\text{Fe(IV)}$  was involved in the degradation reaction, IPA was introduced to do quenching experiments. In Fig. 8a, the blue line indicates the reaction with addition of IPA, which still yields the same ratio of DMPO-OH (blue circle) and HDMPO-OH (red square) characteristic signals. The orange

line indicates that the characteristic signals of DMPO-OH (blue circle) and HDMPO-OH (red square) are still generated after 10 minutes of reaction, which proves that  $\text{Fe(IV)}$  was more likely the main reactive species generated during the catalysis reaction. In order to further confirm the involvement of  $\text{Fe(IV)}$  participation in the reaction, DMPO was used as a spin trap agent and the oxygen transfer reaction of PMSO to  $\text{PMSO}_2$  [40,41] was studied by using UPLC-ESI-tqMS. The reaction results of PMSO are represented by Fig. 8c-f, which correspond to the spectra of PMSO (0.1 mmol/L) before reaction, the spectra of PMSO (0.1 mmol/L) after 10 min reaction with the reactive species generated by Fe-Si-B glassy ribbon and PAA, the monitoring of PMSO<sub>2</sub> before reaction, and the monitoring of PMSO<sub>2</sub> after 10 min reaction with the reactive species generated by Fe-Si-B glassy ribbon and PAA, respectively. From Fig. 8c-d, the retention time of PMSO was 4.0 min, while the peak area of PMSO (0.1 mmol/L) decreased by about 76.16% after reaction, which proved that most of the PMSO was consumed in the process of participating in the reaction. In Fig. 8e-f, there was no PMSO<sub>2</sub> existed before the reaction of PMSO, and after 10 min of reaction, a signal peak of PMSO<sub>2</sub> appeared at 4.1 min, which was consistent with the standard signal of PMSO<sub>2</sub>, proving that  $\text{Fe(IV)}$  existed in the reaction system.

Previous studies [42–44] have identified various reactive species

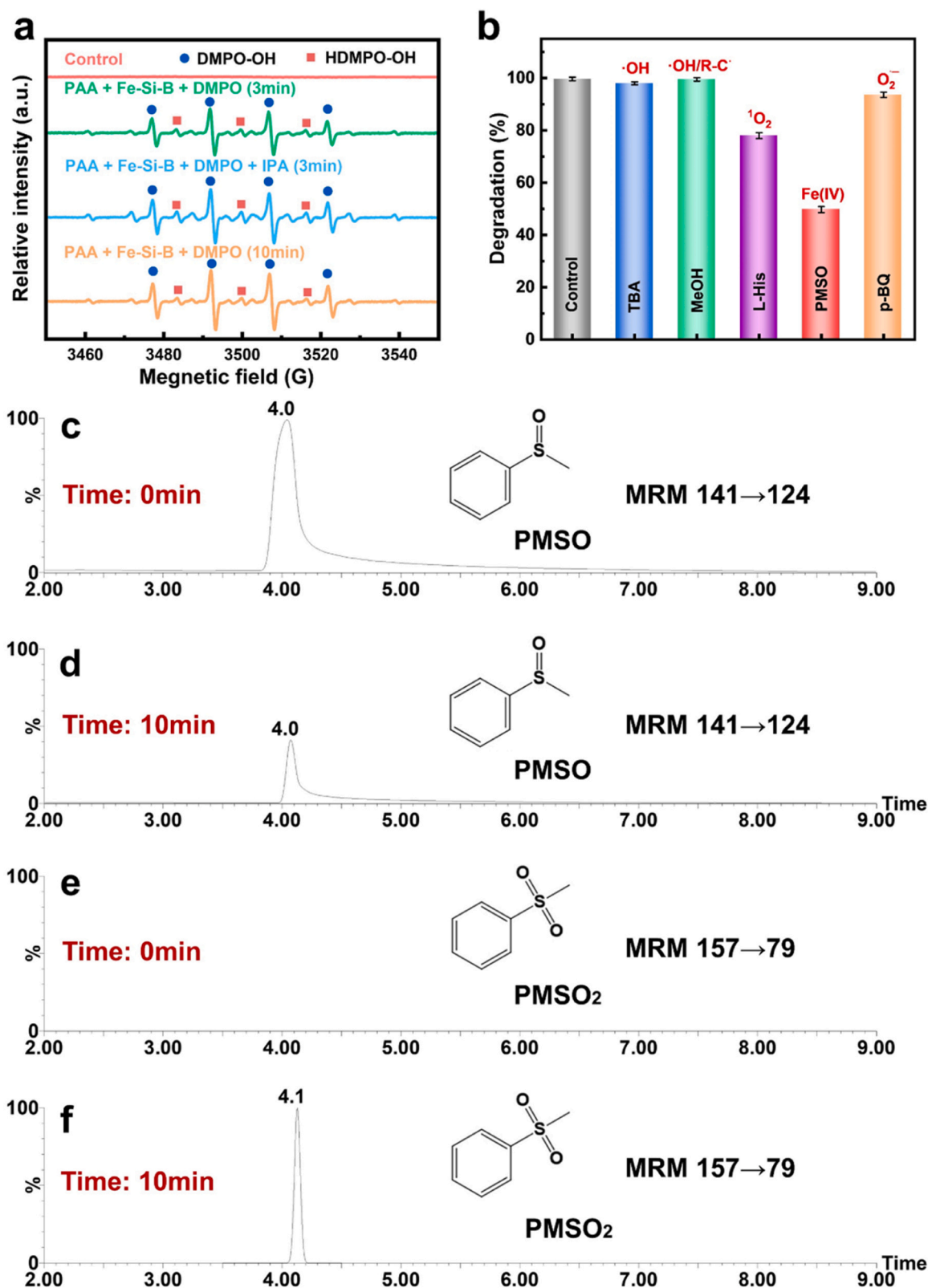


**Fig. 8.** (a) EPR spectra of DMPO-OH and HDMPO-OH generated by PAA activated Fe-Si-B glassy ribbon (PAA = 0.64 mmol/L, Fe-Si-B = 2 g/L, IPA = 13.04 mol/L), (b) Effect of different quenching agents on the catalysis degradation of humic acid by Fe-Si-B glassy ribbon treatment ( $[TBA]_0 = [MeOH]_0 = 100$  mM,  $[L-His]_0 = [p-BQ]_0 = 20$  mM,  $[PMSO]_0 = 5$  mM), (c-f) UPLC-MS/MS MRM spectra of oxidation of PMSO (141→124) and the generation of PMSO<sub>2</sub> (157→79) by Fe-Si-B glassy ribbon-based AOPs (PAA = 10 mg/L, Fe-Si-B = 2 g/L), (c) MRM spectra of PMSO at time = 0 min; (d) MRM spectra of PMSO at time = 10 min, (e) MRM spectra of PMSO<sub>2</sub> at time = 0 min, (f) MRM spectra of PMSO<sub>2</sub> at time = 10 min.

involved in PAA-based AOPs, including free radicals such as  $\bullet\text{OH}$ ,  $\text{R-C}\bullet$  ( $\text{CH}_3\text{C}(\text{O})\text{O}\bullet$ ,  $\text{CH}_3\text{C}(\text{O})\text{OO}\bullet$ ,  $\text{CH}_3\text{OO}\bullet$  and  $\bullet\text{CH}_3$ ),  $^1\text{O}_2$ , and  $\text{O}_2^{\bullet-}$ . To gain deeper insights into the degradation mechanisms in Fe-Si-B glassy ribbon-based AOPs catalyzed by PAA, radical quenching experiments were conducted, as illustrated in Fig. 8b and Fig. S4. The addition of TBA which acts as a scavenger for  $\bullet\text{OH}$  (with a rate constant of  $k_{\bullet\text{OH}/\text{TBA}} = (3.8 - 7.6) \times 10^8 \text{ M}^{-1}\text{s}^{-1}$ ) and MeOH (a scavenger for both  $\bullet\text{OH}$  and  $\text{R-C}\bullet$ ) resulted in NOM degradation contents of 98.0% and 99.5%, respectively. This suggests that  $\bullet\text{OH}$  and  $\text{R-C}\bullet$  are not major contributors to the degradation process. When *p*-BQ (a scavenger for  $\text{O}_2^{\bullet-}$ ) was added, the NOM degradation content reached 93.6%. However, the addition of L-His (a scavenger for  $^1\text{O}_2$ ) led to degradation content of only 78.0%. Interestingly, when PMSO (a scavenger for Fe(IV)) was introduced, the NOM degradation content dropped to 49.7%. These results indicate that Fe(IV) is the main reactive species involved in Fe-Si-B glassy ribbon-based AOPs, followed by  $^1\text{O}_2$  and  $\text{O}_2^{\bullet-}$ .

As a pre-oxidation method, the mechanism of NOM degradation in the Fe-Si-B glassy ribbon-based AOPs can be clarified after fluorescence analysis, material characterization, UPLC-MS analysis, and verification of Fe(IV), which is represented by Fig. 9a-b. NOM, as a ubiquitous substance in nature, can follow rainwater into or infiltrate into rivers and lakes. When water from these rivers and lakes are used as raw water, treatment procedures such as sedimentation, filtration, and disinfection are needed. In this paper, a pre-oxidation process for the degradation of NOM based on Fe-based amorphous alloys (Fig. 9a) is proposed along with the mechanism of NOM degradation (Fig. 9b).

### 3.6. Reusability of Fe-Si-B glassy ribbon

The reusability of a catalyst is indeed a crucial factor in evaluating its potential for practical applications. Fig. 10 illustrates the alterations in surface morphology and physicochemical properties of the Fe-Si-B glassy ribbon after undergoing 1 and 10 cycles of reuse. As depicts in Fig. 10a, it is evident that the pits on the surface of the Fe-Si-B glassy ribbon become more pronounced with each successive cycle. Notably, the amorphous characteristics of the Fe-Si-B glassy ribbon remain

unchanged, regardless of the number of reaction cycles, thereby preserving the advantageous properties of the amorphous alloy. Significantly, Fig. 10b reveals that extensive flaking occurs on the surface of the Fe-Si-B glassy ribbon during experiment. This flaking intensifies uneven stress across the surface, leading to the continuous detachment of Fe(II) and the extension of surface cracks, ultimately resulting in a cracked appearance. These fragments continually expose fresh contact surfaces, enhancing the interaction area with reactants. Concurrently, unique nano-patterns forming within these cracks expand the reactive surface area, thereby sustaining or potentially augmenting the effectiveness of humic acid degradation. Additionally, EDS analysis (as illustrated in Fig. 10c) indicates that after multiple recycling processes, the atomic ratio of Fe to Si in the Fe-Si-B glassy ribbon remains relatively consistent. Specifically, post-cycling, this ratio stands at Fe: Si = 35.55: 3.91, which, even after 10 cycles, closely aligns with the pre-reaction atomic ratio of Fe: Si = 81.71: 8.31. This consistency underscores the robust recyclability of the Fe component in the material. The pivotal question is whether the Fe-Si-B glassy ribbon can maintain its Fe(II) content across multiple uses, as Fe(II) is the primary valence state that predominantly generates Fe(IV). The XPS results after 10 reuse cycles reveal that the original sample of Fe-Si-B glassy ribbon exhibited three valence states:  $\text{Fe}^0$  (705.38 eV, 16.06%),  $\text{Fe}^{2+}$  (709.18 eV, 55.25%), and  $\text{Fe}^{3+}$  (711.38 eV, 28.69%). At the completion of the first cycle,  $\text{Fe}^0$  had entirely vanished, with an increase in the percentages of  $\text{Fe}^{2+}$  (64.03%) and  $\text{Fe}^{3+}$  (35.97%). After 10 reuse cycles,  $\text{Fe}^0$  remained absent, and there was a conversion between  $\text{Fe}^{2+}$  (64.64%) and  $\text{Fe}^{3+}$  (35.36%), corroborating the previous findings (Fig. 10d).

The results clearly demonstrate the recyclability of Fe-Si-B glassy ribbon, affirming its potential for repeated use not only in terms of the reaction contact area on its surface but also considering the conditions for elemental conversion. This recyclability significantly enhances the practical applicability of Fe-Si-B glassy ribbon and reduces operational costs, reinforcing its suitability as a catalyst in water treatment applications.

### 3.7. Effect of Fe-Si-B glassy ribbon and $\text{Br}^-$ dosage

In the Fe-Si-B glassy ribbon-based AOPs, PAA reacts with  $\text{Br}^-$  in simulated drinking water to form the secondary oxidant HOBr ( $k = 0.24 \pm 0.02 \text{ M}^{-1} \text{ s}^{-1}$ ), and the secondary oxidant exhibits high reactivity with phenolic organic compounds ( $k = 10^3 - 10^5 \text{ M}^{-1} \text{ s}^{-1}$ ) [45]. At the same time, PAA activates Fe-Si-B glassy ribbon and reacts with Fe(II) to form Fe(IV) ( $k = 63 - 76 \text{ M}^{-1} \text{ s}^{-1}$ ) [46]. In order to explore the competition between Fe-Si-B glassy ribbon and  $\text{Br}^-$  for PAA, the dosage of Fe-Si-B glassy ribbon and  $\text{Br}^-$  was changed, and the results were shown in Fig. 11. No brominated-DBPs can be produced without the presence of  $\text{Br}^-$  (Fig. 11a). The level of TII PIS  $m/z = 79$  increases with the increase of  $\text{Br}^-$  (Fig. 11c), and the production of DBPs also increased. For example,  $\text{Br}_2\text{CHCOOH}$  ( $m/z = 215/217/219$ ) was undetectable before the reaction, and a peak signal was generated with the addition of  $\text{Br}^-$ , and the peak area also increased after the  $\text{Br}^-$  dose was increased. With the participation of  $\text{Br}^-$ , the dose of Fe-Si-B glassy ribbon will also affect the production of DBPs. Fig. 11b shows that the peak area of DBPs decrease with the increase of Fe-Si-B glassy ribbon, and the level of TII PIS  $m/z = 79$  shows a decreasing trend (Fig. 11d). In this process, the increase of  $\text{Br}^-$  dose will react with PAA to produce more secondary oxidants, which in turn react with humic acid to produce more DBPs. The increase in the dosage of Fe-Si-B glassy ribbon, when reacted with PAA, leads to the production of a greater amount of Fe(IV). This, in turn, results in a more comprehensive degradation of humic acid. In summary, there is competition between the reaction of  $\text{Br}^-$  to produce secondary oxidant and Fe-Si-B glassy ribbon to Fe(IV) in the system, and the formation of secondary oxidant and Fe(IV) will affect the formation of DBPs.

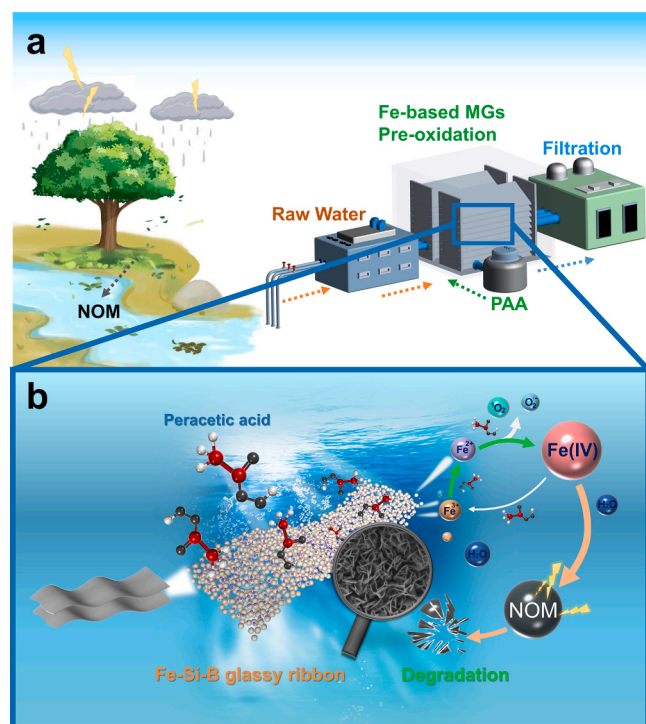
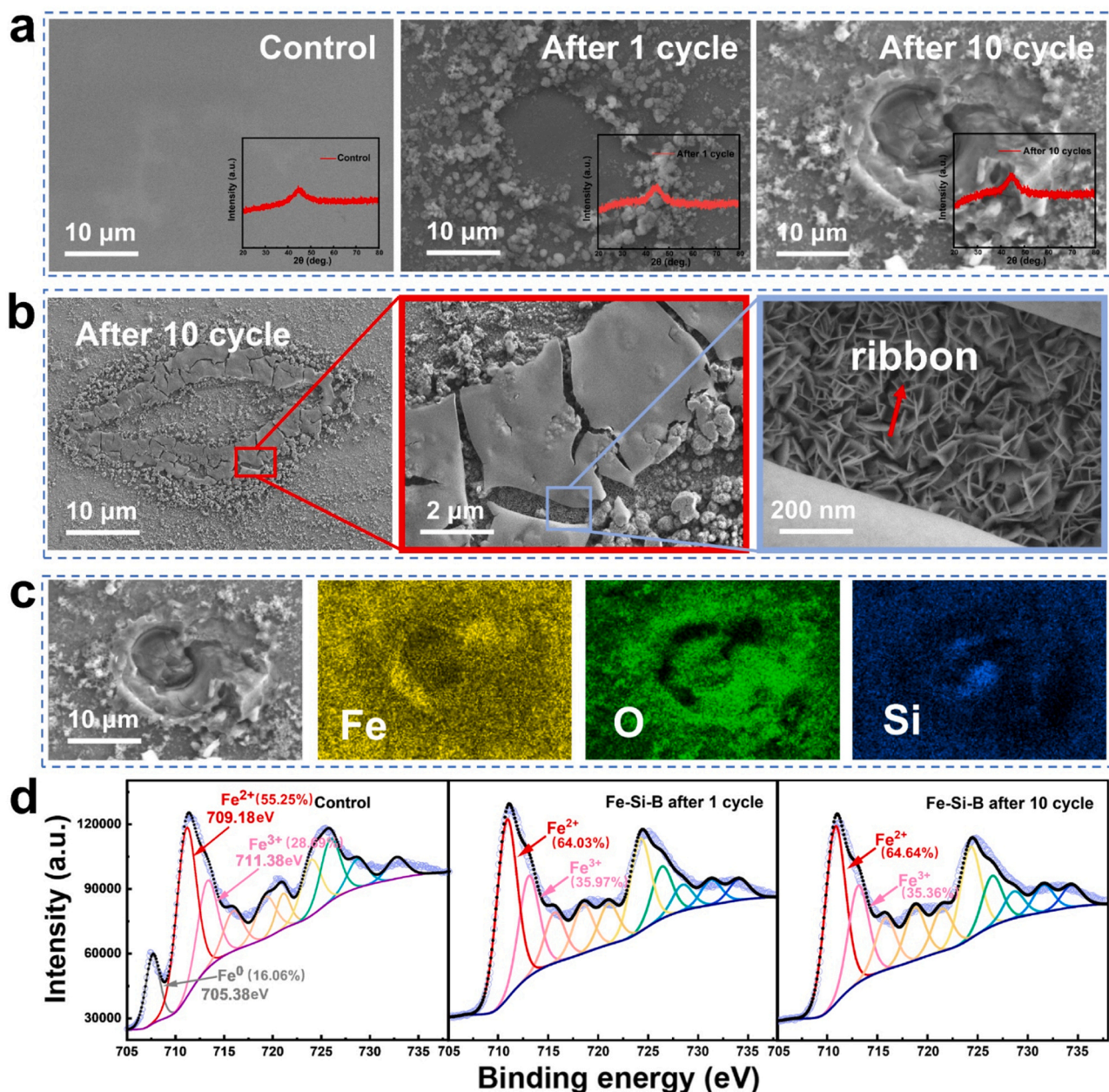


Fig. 9. (a) Schematic graph of pre-oxidation water treatment equipment based on Fe-Si-B glassy ribbon, (b) Mechanism of Fe-Si-B glassy ribbon-based AOPs.





**Fig. 10.** (a) The SEM image of the as-received Fe-Si-B glassy ribbon, and Fe-Si-B glassy ribbon after catalysis reaction with PAA (10 mg/L) after once and 10th reaction cycle, (b) The enlarged SEM image of Fe-Si-B glassy ribbon after catalysis reaction with PAA (10 mg/L) after 10th reaction cycle, (c) The EDS mapping result of Fe-Si-B glassy ribbon after catalysis reaction with PAA (10 mg/L) after 10th reaction cycle, (d) The XPS spectra of Fe 2p for the as-received Fe-Si-B glassy ribbon, and Fe-Si-B glassy ribbon after catalysis reaction with PAA (10 mg/L) after once and 10th reaction cycle.

### 3.8. Continuous flow experiments and overall toxicity evaluations

For practical applications of Fe-Si-B glassy ribbon-based AOPs, continuous flow experiments were conducted to assess both humic acid degradation and the control of DBPs formation. Additionally, overall toxicity evaluations were performed using luminescent bacteria. The continuous flow experiments were set up using a peristaltic pump (Fig. 12a) to circulate the treated water at a flow rate of 2 mL/s. Fig. 12b illustrates the degradation process of NOM under both motionless (normal exposure) and continuous flow conditions. The results reveal a consistent degradation rate of humic acid across both experimental setups. Regarding the control of DBPs, the levels of DBPs produced in the continuous flow experiments were significantly lower than those generated by PAA disinfection without Fe-Si-B glassy ribbon treatment (Fig. S5). After a 2-hour treatment, only 4.60% of residual DBPs

remained (Fig. 12c), indicating that Fe-Si-B glassy ribbon-based AOPs hold promise for effective DBPs formation control.

To determine if the toxicity aligned with the chemical degradation process, the overall toxicity of the reaction solution was assessed by using luminescent bacteria *Vibrio fischeri* (Fig. 12d). As depicted in Fig. 12e, when luminescent bacteria were exposed to the initial simulated drinking water sample containing 3 mg/L humic acid, 2 mg/L Br<sup>-</sup>, and 10 mg/L PAA disinfectant, an inhibition rate of 38.72% was observed. As degradation progressed, the inhibition rate of the luminescent bacteria gradually decreased. After 2.5 h of reaction time, the inhibition rate of *Vibrio fischeri* dropped to 21.64%, indicating a reduction in overall toxicity during the degradation process. By the time the reaction had reached 24 h and 36 h, the inhibition rate had significantly declined to 1.04% and 0.26%, respectively, virtually eliminating the toxicity to bacteria. It's noteworthy that the biotoxicity degradation

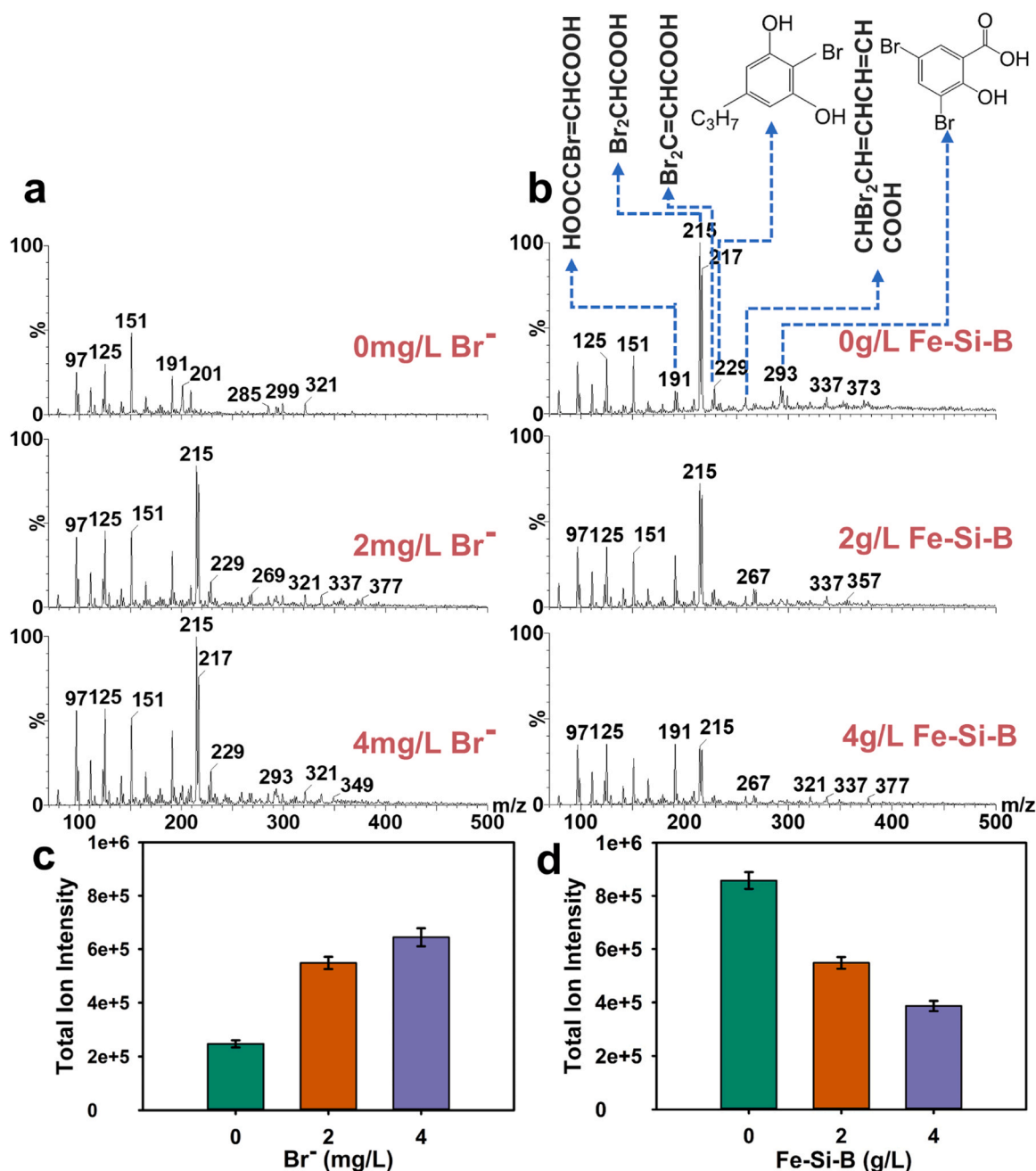


**Fig. 11.** (a) UPLC-MS/MS PIS spectra of  $m/z = 79$  of simulated raw water by PAA disinfection (10 mg/L) in the presence of 2 g/L Fe-Si-B glassy ribbon and  $\text{Br}^-$  (0, 2, and 4 mg/L), (b) UPLC-MS/MS PIS spectra of  $m/z = 79$  of simulated raw water by PAA disinfection (10 mg/L) in the presence of  $\text{Br}^-$  (2 mg/L) and Fe-Si-B glassy ribbon (0, 2, and 4 g/L Fe-Si-B glassy ribbon), (c) the TII level of (a), (d) the TII level of (b).

process is slower than the chemical degradation process. Furthermore, the quantification of Fe and Si leaching from the Fe-based amorphous alloys was conducted using ICP-OES, and the results are presented in Table 2. To provide a basis for comparison, Fe powder was used as a homogeneous system. The results revealed that the concentration of Fe in the reaction solution following treatment with the Fe-Si-B glassy ribbon was 0.146 mg/L, which is lower than that observed with the homogeneous Fe powder (0.304 mg/L). Additionally, the concentration of Si leached from the Fe-Si-B glassy ribbon was relatively low, at 0.128 mg/L.

In summary, the continuous flow experiments and toxicity evaluations of Fe-Si-B glassy ribbon-based AOPs demonstrate promising performance in both chemical degradation and biotoxicity reduction, accompanied by lower levels of metal leaching, highlighting their

potential for practical applications.

#### 4. Conclusions

In conclusion, the use of PAA as an oxidant in conjunction with Fe-Si-B glassy ribbon has proven to be highly effective in inducing the formation of fine nanoflower structures, significantly enhancing the catalysis efficiency. Fluorescence experiments conducted to examine the degradation trends of humic acid by Fe-Si-B glassy ribbon-based AOPs revealed their ability to rapidly degrade humic acid within 30 minutes. Comparative fluorescence experiments assessing the degradation of humic acid using  $\text{Cl}_2$ , PAA, and Fe-Si-B glassy ribbon-based AOPs indicated that the latter exhibited markedly superior degradation performance, achieving a degradation rate of 98.21%. This superiority was

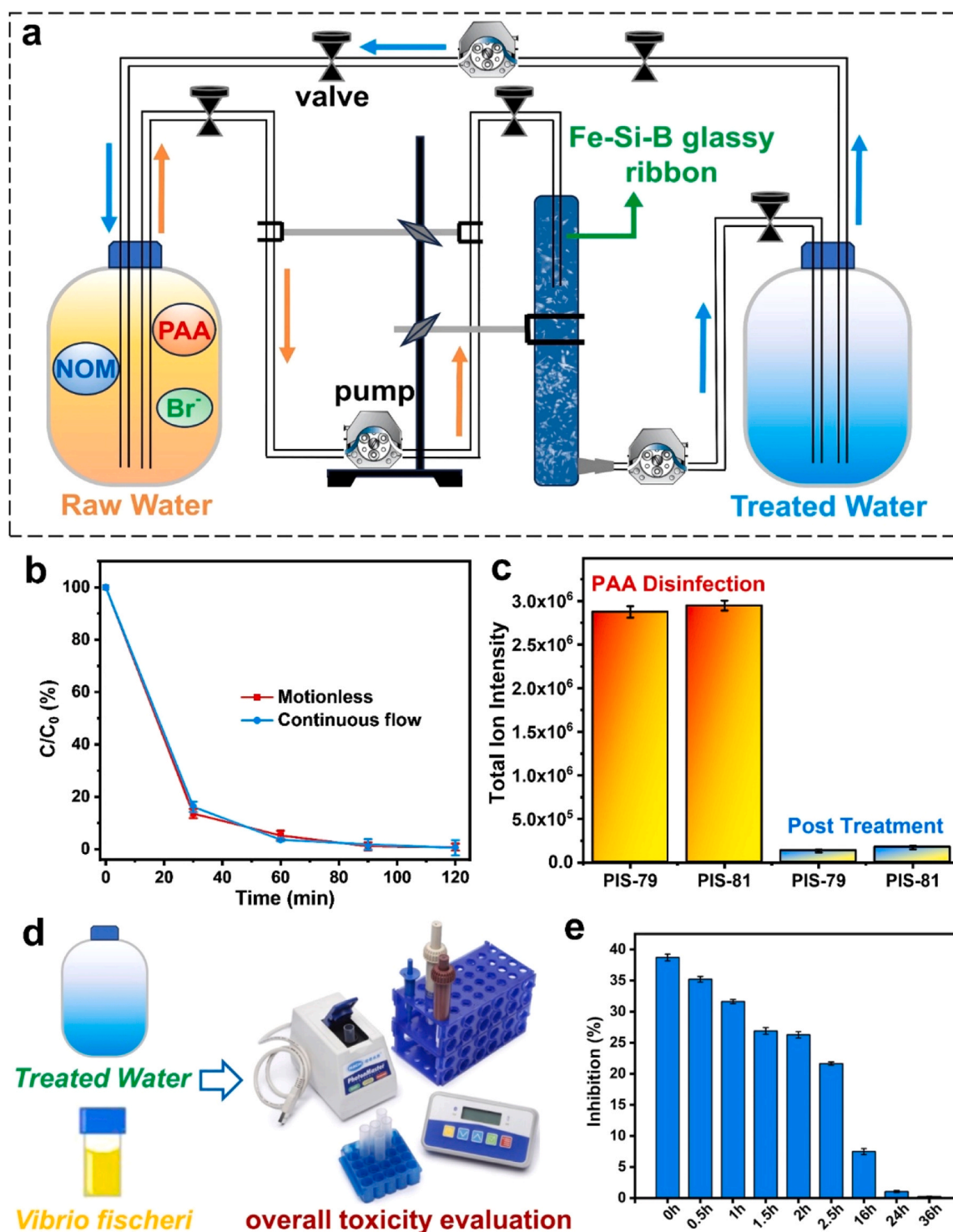


**Fig. 12.** (a) Schematic diagram of continuous flow test of Fe-Si-B glassy ribbon-based AOPs (10 mg/L PAA, 2 g/L Fe-Si-B glassy ribbon, flow rate of 2 mL/s), (b) Comparison of humic acid degradation by motionless and continuous flow of Fe-Si-B glassy ribbon-based AOPs, (c) TII<sub>PIS-79</sub> and TII<sub>PIS-81</sub> of DBPs generated before and after glassy ribbon treatment, (d) Schematic diagram of overall toxicity evaluation, (e) Inhibition of luminescent bacteria (*Vibrio fischeri*) at different time intervals of glassy ribbon treatment process.

further underscored by UPLC-MS analysis of DBPs, showing that Fe-Si-B glassy ribbon-based AOPs produced fewer DBPs under identical conditions that 80.64% generated DBPs can be removed compared with no treatment. Material characterization involving EDS and XPS after treating Fe-Si-B glassy ribbon with varying doses of PAA revealed notable changes in elemental composition, particularly in iron, which was predominantly converted into Fe(IV). This conversion, confirmed

through EPR experiments and PMSO oxygen exchange reactions, facilitated the accelerated degradation of humic acid. The cycling performance of Fe-Si-B glassy ribbon as a catalyst was evaluated, demonstrating its good recyclability. Notably, after 10 cycles, the formation of nanoflower structures and the galvanic cell effect in Fe-Si-B glassy ribbon-based AOPs resulted in more thorough degradation of humic acid. However, a competitive reaction involving the formation of



**Table 2**

The amount of Fe and Si leached from Fe-Si-B glassy ribbon and Fe powder treatment.

Element	Fe-Si-B glassy ribbon treatment (mg/L)	Fe powder treatment (mg/L)
Fe	0.146	0.304
Si	0.128	—

secondary oxidants from Br<sup>-</sup> and the generation of Fe(IV) for humic acid degradation was observed. The balance between the dosages of Br<sup>-</sup> and Fe-Si-B glassy ribbon is crucial for optimizing degradation efficiency. The continuous flow experiments and toxicity evaluations of Fe-Si-B glassy ribbon-based AOPs demonstrate promising performance in both chemical degradation and biotoxicity reduction, accompanied by lower levels of metal leaching. Overall, Fe-Si-B glassy ribbon combined with PAA represents a highly effective nanoengineered system for the degradation of humic acid, offering a promising alternative solution for drinking water treatment.

### CRediT authorship contribution statement

**Yan Liu:** Formal analysis. **Yangguang Zhan:** Investigation. **Yu Zhang:** Investigation. **Xingran Zhao:** Investigation. **Jiang Ma:** Writing – review & editing, Supervision, Resources, Funding acquisition, Conceptualization. **Yujian Li:** Writing – original draft, Investigation, Formal analysis, Data curation. **Mengting Yang:** Formal analysis, Conceptualization. **Wenqing Ruan:** Formal analysis. **Zhenxuan Zhang:** Writing – review & editing, Supervision, Methodology, Funding acquisition, Formal analysis, Conceptualization. **Xiong Liang:** Writing – review & editing, Supervision, Resources, Funding acquisition.

### Declaration of Competing Interest

The authors declare that they have no known competing financial interests or personal relationships that could have appeared to influence the work reported in this paper.

### Data Availability

Data will be made available on request.

### Acknowledgments

The work was supported by the Key Basic and Applied Research Program of Guangdong Province, China (Grant No. 2019B030302010), Guangdong Basic and Applied Basic Research Foundation (Grant No. 2020B1515120092), the National Natural Science Foundation of China (Grant No. 52122105, 51971150, 52271150, 52201185), the National Key Research and Development Program of China (Grant No. 2018YFA0703605). The authors thank the assistance on microscope observation received from the Electron Microscope Center of the Shenzhen University. We would also like to thank the anonymous reviewers for their valuable suggestions.

### Appendix A. Supporting information

Supplementary data associated with this article can be found in the online version at [doi:10.1016/j.apcatb.2024.124161](https://doi.org/10.1016/j.apcatb.2024.124161).

### References

- [1] D. Gogoi, R.S. Karmur, M.R. Das, N.N. Ghosh, Cu and CoFe<sub>2</sub>O<sub>4</sub> nanoparticles decorated hierarchical porous carbon: An excellent catalyst for reduction of nitroaromatics and microwave-assisted antibiotic degradation, *Appl. Catal., B* 312 (2022) 121407.

- [2] S. Koley, S. Dash, M. Khwairakpam, A.S. Kalamdhad, Perspectives and understanding on the occurrence, toxicity and abatement technologies of disinfection by-products in drinking water, *J. Environ. Manag.* 351 (2024) 119770.
- [3] H. Liu, Y. Li, H. Yang, M.S. Siddique, W. Yu, The characters of dissolved organic matters from litter-mimic with the different humification states and their effects on drinking water treatment processes, *Sci. Total Environ.* 861 (2023) 160470.
- [4] J. Jiang, X. Zhang, X. Zhu, Y. Li, Removal of intermediate aromatic halogenated DBPs by activated carbon adsorption: a new approach to controlling halogenated DBPs in chlorinated drinking water, *Environ. Sci. Technol.* 51 (2017) 3435–3444.
- [5] W.D. King, L.D. Marrett, C.G. Woolcott, Case-control study of colon and rectal cancers and chlorination by-products in treated water, *Cancer Epidemiol. Biomarkers* 9 (2000) 813–818.
- [6] A. Zhang, F. Wang, W. Chu, X. Yang, Y. Pan, H. Zhu, Integrated control of CX<sub>3</sub>R-type DBP formation by coupling thermally activated persulfate pre-oxidation and chloramination, *Water Res.* 160 (2019) 304–312.
- [7] M. Kitis, Disinfection of wastewater with peracetic acid: a review, *Environ. Int.* 30 (2004) 47–55.
- [8] L.L. Zhang, J.B. Chen, Y.L. Zhang, Z.J. Yu, R.C. Ji, X.F. Zhou, Activation of peracetic acid with cobalt anchored on 2D sandwich-like MXenes (Co@MXenes) for organic contaminant degradation: high efficiency and contribution of acetylperoxyl radicals, *Appl. Catal., B* 297 (2021) 120475.
- [9] X.-W. Ao, J. Eloranta, C.-H. Huang, D. Santoro, W.-J. Sun, Z.-D. Lu, C. Li, Peracetic acid-based advanced oxidation processes for decontamination and disinfection of water: a review, *Water Res.* 188 (2021) 116479.
- [10] L. Meng, J. Chen, D. Kong, Y. Ji, J. Lu, X. Yin, Q. Zhou, Transformation of bromide and formation of brominated disinfection byproducts in peracetic acid oxidation of phenol, *Chemosphere* 291 (2022) 132698.
- [11] C. Liu, D.-W. Chen, Y.-Y. Ren, W. Chen, Removal efficiency and mechanism of phycocyanin in water by zero-valent iron, *Chemosphere* 218 (2019) 402–411.
- [12] Y. Chen, L. Long, Y. Luo, B. Zeng, Z. Liu, Q. Shao, F. Wu, P. Xie, J. Ma, Insights into persulfate activation by FeO for phenol removal: the production and effect of Fe(IV), *Chem. Eng. J.* 468 (2023) 143842.
- [13] Y. Sun, Z.X. Yang, P.F. Tian, Y.Y. Sheng, J. Xu, Y.F. Han, Oxidative degradation of nitrobenzene by a Fenton-like reaction with Fe-Cu bimetallic catalysts, *Appl. Catal., B* 244 (2019) 1–10.
- [14] J. Li, Y.J. Wan, Y.J. Li, G. Yao, B. Lai, Surface Fe(III)/Fe(II) cycle promoted the degradation of atrazine by peroxymonosulfate activation in the presence of hydroxylamine, *Appl. Catal., B* 256 (2019) 117782.
- [15] W.H. Wang, Bulk metallic glasses with functional physical properties, *Adv. Mater.* 21 (2009) 4524–4544.
- [16] Z. Jia, X. Duan, P. Qin, W. Zhang, W. Wang, C. Yang, H. Sun, S. Wang, L.-C. Zhang, Disordered atomic packing structure of metallic glass: toward ultrafast hydroxyl radicals production rate and strong electron transfer ability in catalytic performance, *Adv. Funct. Mater.* 27 (2017) 1702258.
- [17] Z. Jia, Q. Wang, L. Sun, Q. Wang, L.-C. Zhang, G. Wu, J.-H. Luan, Z.-B. Jiao, A. Wang, S.-X. Liang, M. Gu, J. Lu, Attractive in situ self-reconstructed hierarchical gradient structure of metallic glass for high efficiency and remarkable stability in catalytic performance, *Adv. Funct. Mater.* 29 (2019) 1807857.
- [18] L. Zhang, L. Qiu, Q. Zhu, X. Liang, J. Huang, M. Yang, Z. Zhang, J. Ma, J. Shen, Insight into efficient degradation of 3,5-dichlorosalicylic acid by Fe-Si-B amorphous ribbon under neutral condition, *Appl. Catal., B* 294 (2021) 120258.
- [19] L.-C. Zhang, S.-X. Liang, Fe-based metallic glasses in functional catalytic applications, *Chem. – Asian J.* 13 (2018) 3575–3592.
- [20] L.-C. Zhang, Z. Jia, F. Lyu, S.-X. Liang, J. Lu, A review of catalytic performance of metallic glasses in wastewater treatment: Recent progress and prospects, *Prog. Mater. Sci.* 105 (2019) 100576.
- [21] H. Zhai, X. Zhang, Formation and decomposition of new and unknown polar brominated disinfection byproducts during chlorination, *Environ. Sci. Technol.* 45 (2011) 2194–2201.
- [22] S. Gligorovski, R. Strekowski, S. Barbati, D. Vione, Environmental implications of hydroxyl radicals (•OH), *Chem. Rev.* 115 (2015) 13051–13092.
- [23] G. Kresse, J. Hafner, Ab initio molecular dynamics for liquid metals, *Phys. Rev. B* 1993 47 (1993) 558–561.
- [24] J. Iniguez, D. Vanderbilt, L. Bellaiche, First-principles study of (BiScO<sub>3</sub>)<sub>1-x</sub>–(PbTiO<sub>3</sub>)<sub>x</sub> piezoelectric alloys, *Phys. Rev. B* 67 (2003) 224107.
- [25] B. Hammer, L.B. Hansen, J.K. Nørskov, Improved adsorption energetics within density-functional theory using revised Perdew-Burke-Ernzerhof functionals, *Phys. Rev. B* 59 (1999) 7413.
- [26] R. Asahi, W. Mannstadt, A.J. Freeman, Optical properties and electronic structures of semiconductors with screened-exchange LDA, *Phys. Rev. B* 59 (1999) 7486.
- [27] J.P. Perdew, K. Burke, M. Ernzerhof, Generalized gradient approximation made simple, *Phys. Rev. Lett.* 77 (1996) 3865.
- [28] J.P. Perdew, A. Ruzsinszky, G.I. Csonka, O.A. Vydrov, G.E. Scuseria, L. A. Constantin, X. Zhou, K. Burke, Restoring the density-gradient expansion for exchange in solids and surfaces, *Phys. Rev. Lett.* 100 (2008) 136406.
- [29] P.E. Blöchl, Projector augmented-wave method, *Phys. Rev. B* 50 (1994) 17953.
- [30] G.I. Csonka, J.P. Perdew, A. Ruzsinszky, P.H. Phillips, S. Lebègue, J. Paier, O. A. Vydrov, J.G. Ángyán, Assessing the performance of recent density functionals for bulk solids, *Phys. Rev. B* 79 (2009) 155107.
- [31] M. Abbas, M. Adil, S. Ehtisham-ul-Haque, B. Munir, M. Yameen, A. Ghaffar, G. A. Shar, M. Asif Tahir, M. Iqbal, *Vibrio fischeri* bioluminescence inhibition assay for ecotoxicity assessment: a review, *Sci. Total Environ.* 626 (2018) 1295–1309.
- [32] W. Chen, P. Westerhoff, J.A. Leenheer, K. Booksh, Fluorescence excitation - emission matrix regional integration to quantify spectra for dissolved organic matter, *Environ. Sci. Technol.* 37 (2003) 5701–5710.

- [33] S. Monarca, C. Zani, S.D. Richardson, A.D. Thruston, M. Moretti, D. Feretti, M. Villarini, A new approach to evaluating the toxicity of genotoxicity of disinfected drinking water, *Water Res* 38 (2004) 3809–3819.
- [34] M. Yang, X. Zhang, Q. Liang, B. Yang, Application of (LC/MS/MS precursor ion scan for evaluating the occurrence, formation and control of polar halogenated DBPs in disinfected waters: a review, *Water Res* 158 (2019) 322–337.
- [35] S.M. Ponder, J.G. Darab, J. Bucher, D. Caulder, I. Craig, L. Davis, N. Edelstein, W. Lukens, H. Nitsche, L. Rao, D.K. Shuh, T.E. Mallouk, Surface chemistry and electrochemistry of supported zerovalent iron nanoparticles in the remediation of aqueous metal contaminants, *Chem. Mater.* 13 (2001) 479–486.
- [36] Y. Tang, Y. Shao, N. Chen, K.-F. Yao, Rapid decomposition of direct blue 6 in neutral solution by Fe–B amorphous alloys, *RSC Adv.* 5 (2015) 6215–6221.
- [37] P. Zhou, Y. Yang, W. Ren, X. Li, Y. Zhang, B. Lai, S. Wang, X. Duan, Molecular and kinetic insights to boron boosted Fenton-like activation of peroxymonosulfate for water decontamination, *Appl. Catal. B* 319 (2022) 121916.
- [38] F. Chen, L.-L. Liu, J.-J. Chen, W.-W. Li, Y.-P. Chen, Y.-J. Zhang, J.-H. Wu, S.-C. Mei, Q. Yang, H.-Q. Yu, Efficient decontamination of organic pollutants under high salinity conditions by a nonradical peroxymonosulfate activation system, *Water Res* 191 (2021) 116799.
- [39] Z. Qi, Q. Zhang, D. Zhu, Z. Ding, J. Niu, D. Liu, Y. Zhao, Y. Xia, Z. Zhao, X. Wang, The reaction pathways of  $\text{H}_2\text{O}_2(\text{aq})$  in the He plasma jet with a liquid system, *Plasma Chem. Plasma P.* 40 (2020) 1001–1018.
- [40] Z. Wang, W. Qiu, S.-Y. Pang, Y. Zhou, Y. Gan, C. Guan, J. Jiang, Further understanding the involvement of Fe(IV) in peroxydisulfate and peroxymonosulfate activation by Fe(II) for oxidative water treatment, *Chem. Eng. J.* 371 (2019) 842–847.
- [41] O. Pestovsky, A. Bakac, Aqueous ferryl(IV) ion: kinetics of oxygen atom transfer to substrates and oxo exchange with solvent water, *Inorg. Chem.* 45 (2006) 814–820.
- [42] X. Jiang, B. Zhou, W. Yang, J. Chen, C. Miao, Z. Guo, H. Li, Y. Hou, X. Xu, L. Zhu, D. Lin, J. Xu, Precise coordination of high-loading Fe single atoms with sulfur boosts selective generation of nonradicals, *Proc. Natl. Acad. Sci.* 121 (2024) e2309102121.
- [43] Z. Yu, J. Wu, J. Zhang, X. Chen, Z. Wang, Y. Zhang, D. Li, J. Chen, H. Liu, P. Chen, W. Lv, G. Liu, Carbon nitride nanotubes anchored with Cu(I) triggers peracetic acid activation with visible light for removal of antibiotic contaminants: probing mechanisms of non-radical pathways and identifying active sites, *J. Hazard. Mater.* 460 (2023) 132401.
- [44] J. Xiao, Y. Li, H. Dong, Z. Pang, M. Zhao, D. Huang, J. Dong, L. Li, Highly efficient activation of peracetic acid via zero-valent iron-copper bimetallic nanoparticles (nZVI/Cu) for the oxidation of sulfamethazine in aqueous solution under neutral condition, *Appl. Catal., B* 340 (2024) 123183.
- [45] A.D. Shah, Z.-Q. Liu, E. Salhi, T. Hofer, U. von Gunten, Peracetic acid oxidation of saline waters in the absence and presence of  $\text{H}_2\text{O}_2$ : secondary oxidant and disinfection byproduct formation, *Environ. Sci. Technol.* 49 (2015) 1698–1705.
- [46] J. De Laat, H. Gallard, S. Ancelin, B. Legube, Comparative study of the oxidation of atrazine and acetone by  $\text{H}_2\text{O}_2/\text{UV}$ , Fe(III)/UV, Fe(III)/ $\text{H}_2\text{O}_2/\text{UV}$  and Fe(II) or Fe(III)/ $\text{H}_2\text{O}_2$ , *Chemosphere* 39 (1999) 2693–2706.